

Topological Transport and Shape Control of Colloidal Assemblies

Master Thesis in the Physics Degree Program by

Jonas Elschner

Supervised by

Prof. Dr. Thomas M. Fischer

and

Dr. Anna M. E. B. Rossi

Experimental Physics X

Department of Physics, University of Bayreuth

Reviewers:

Prof. Dr. Thomas M. Fischer and Prof. Dr. Daniel de las Heras

Submitted 20.03.2025

Abstract

Exploring different modes of movement is interesting for children as well as for physicists. Amongst other things, both apply toy models for their studies, simplified and often scaled down compared to their real-world analogues. The toy models used in this project are assemblies of paramagnetic colloidal particles, for some of which - colloidal bipeds with a rod shape - a combination of walking and sliding motion has already been realized by means of topological transport [6]. Childlike curiosity in light of these results leads to the question whether other movements are also possible. In this work I show the answer is yes: Applying a superposition of a low- and a high-frequency magnetic field, colloidal bipeds can be made walk and slide independently on a magnetic stripe pattern, which I demonstrate experimentally and underpin with theory and simulation. Furthermore, I present experiments with either a varied magnetic pattern [7] or a varied high-frequency magnetic field, in which the rigidity of the assemblies is broken such that sliding colloidal bipeds are divided, or non-rod-shaped assemblies are formed and exhibit a third mode of movement: swimming. These results show, or suggest, how a time-periodic modulation of foothold and orientation, or shape, can lead to a displacement in a space-periodic environment. I suppose the concepts for sliding and walking here developed based on [5] to be also applicable in corresponding environments in our macroscopic world, e. g. on escalators and stairs. The colloidal assemblies' division and shape change still remain to be investigated thoroughly but might be related to that of cells and other active particles at low Reynolds numbers.

Zusammenfassung

Verschiedene Bewegungsarten zu entdecken, ist sowohl für Kinder als auch für Physiker*innen interessant. Für ihre Studien verwenden beide unter anderem Spielzeugmodelle, vereinfacht und oft verkleinert im Vergleich zu ihren Analoga in der realen Welt. Die Spielzeugmodelle in diesem Projekt sind Strukturen aus paramagnetischen kolloidalen Partikeln, für derer manche - stäbchenförmige kolloidale *Bipeds* - bereits eine Kombination aus Lauf- und Gleitbewegung mittels topologischen Transports realisiert wurde [6]. Angesichts dieser Ergebnisse führt kindliche Neugier auf die Frage, ob andere Bewegungsarten auch möglich sind. In dieser Arbeit bejahe ich die Frage: Unter Einsatz einer Überlagerung eines hoch- und eines niederfrequenten Magnetfelds können kolloidale Bipeds auf einem magnetischen Streifenmuster unabhängig voneinander zum Laufen und zum Gleiten gebracht werden, was ich mit Experimenten demonstriere und mit Theorie und Simulation untermauere. Ferner zeige ich Experimente entweder mit einem abgewandelten magnetischen Muster [7] oder einem abgewandelten hochfrequenten Magnetfeld, in welchem die Starrheit der Strukturen gebrochen wird; so werden gleitende kolloidale Bipeds gespalten, oder nicht stäbchenförmige Strukturen formen sich und zeigen eine dritte Art der Bewegung: schwimmen. Diese Ergebnisse zeigen, oder legen nahe, wie eine zeitlich periodische Modulation von Bodenhaftung und Orientierung, oder der Form, zur Fortbewegung in einer räumlich periodischen Umgebung führen kann. Ich nehme an, dass die auf Basis von [5] entwickelten Konzepte zur Beschreibung von Laufen und Gleiten auch in entsprechenden Umgebungen in unserer makroskopischen Welt anwendbar sind, z. B. auf (Roll-)Treppen. Die Teilung und Formveränderung der kolloidalen Strukturen bleibt noch gründlich zu untersuchen, könnte aber in Zusammenhang mit jener von Zellen und anderen aktiven Teilchen bei niedrigen Reynoldszahlen stehen.

Contents

1 Introduction	5
2 Background	7
2.1 Setup	7
2.2 Adiabatic and robust transport	8
2.3 Topological transport	11
3 Zeroth order, or: how to move	13
3.1 Shaping and orienting agile bipeds	13
3.2 Simulations: sliding and walking	16
3.3 Rolling wheel rule	16
3.4 Calculation of the potential	19
3.5 Theory: Control fence for the stripe pattern	23
3.5.1 Result and heuristical argument	23
3.5.2 Derivation	26
3.6 Experiments: Investigation of the transport modes	29
3.6.1 Sliding and walking: design of control loops	29
3.6.2 Sliding and walking: results	29
3.6.3 Treadmill and dancing	36
4 First order, or: how to break and glue	39
4.1 Experimental result: dividing bipeds	39
4.2 Lessons from the parameter studies	41
4.3 Outlook: joining bipeds	42
5 Higher orders, or: how to change	43
6 Discussion and outlook	45
7 Acknowledgements	46
8 Erklärung/Declaration	47

1 Introduction

Time flies. Now, having reached the end of my studies, I often find myself reviewing the past years at university, becoming aware what I have experienced and learned during that time. And, going back further, I see that each of the previous stations I remember – voluntary service, school, and kindergarten – have given me something and made me grow up a bit.

Luckily, there are also some things that haven't changed so much. I still like playing, especially with moving toys. Surely I am not the only one still fascinated by model cars, walking robots or boats. Now, as a physics student I can justify using them: The toys help understanding how their real-world analogues work. But honestly, as in my childhood it is also just fun to play with them.

This already summarizes the motivation behind the present Master's project, where I have dealt with assemblies of paramagnetic colloidal particles (see Figure 1c) and made them propel in different ways. Let me give a short outline: The assemblies hold together thanks to the magnetic dipolar interaction between the single particles, induced by a high-frequency magnetic field. This field, as we will see later, allows for controlling the *orientation* and the *shape* of the assemblies. The playground where I have placed the particles is a substrate with a static, spatially periodic magnetic pattern (also seen in Figure 1c). The *foothold* of the assemblies is controlled by a low-frequency magnetic field. We are discussing this in Section 2.

In Section 3, we will look into the case where the high-frequency field is *oscillating* and makes our toys, the assemblies, rod-shaped. We will see that they are then able to walk (like humans on solid ground) and slide (like humans being carried with an escalator) independently. This makes them similar to, but more agile than the bipeds investigated by Mahla Mirzaee-Kakhki [5], a former member of Thomas Fischer's group. Therefore we will call them *agile bipeds*.

Furthermore, the assemblies can be made even more agile and interesting by going away from the rigid rod shape. We will see that in Section 4, which deals with the division and joining of bipeds, and in Section 5, where we shortly dive into a swimming-like motion of non-rod-shaped assemblies arising when the high-frequency field is *rotating*.

Before we finally arrive at this point of a partially independent control of shape and transport, which is the current front of this research project, let us now look into some background information on the setup and the concept of topological transport. This is crucial for the entire project.

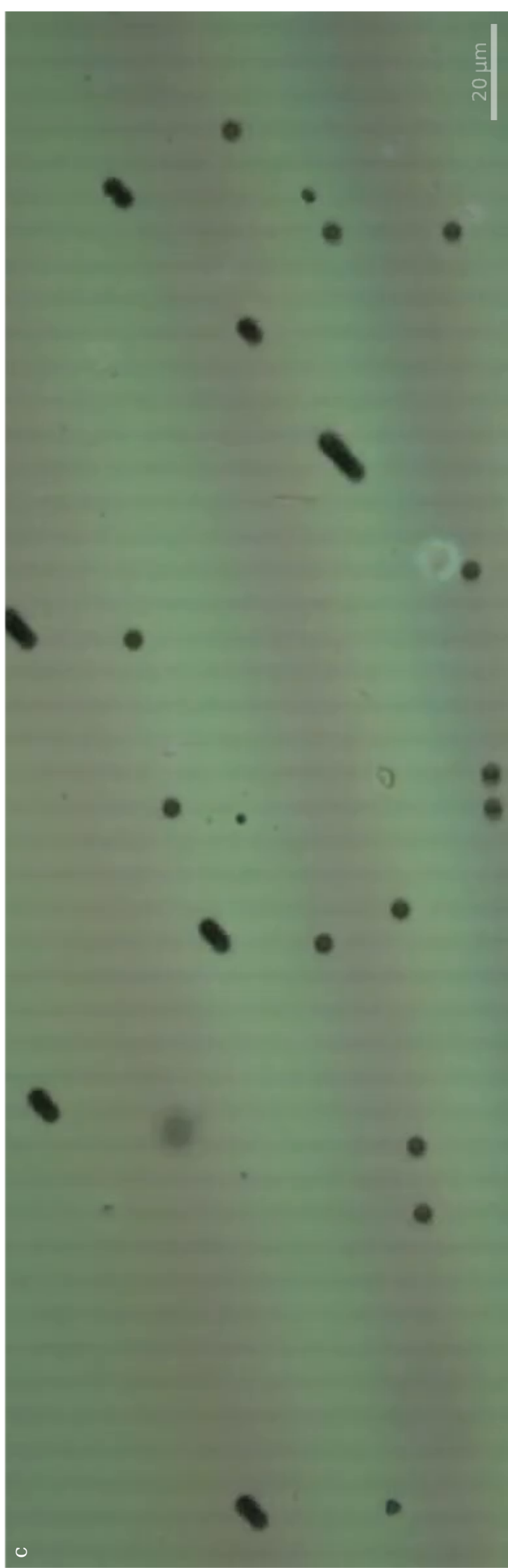
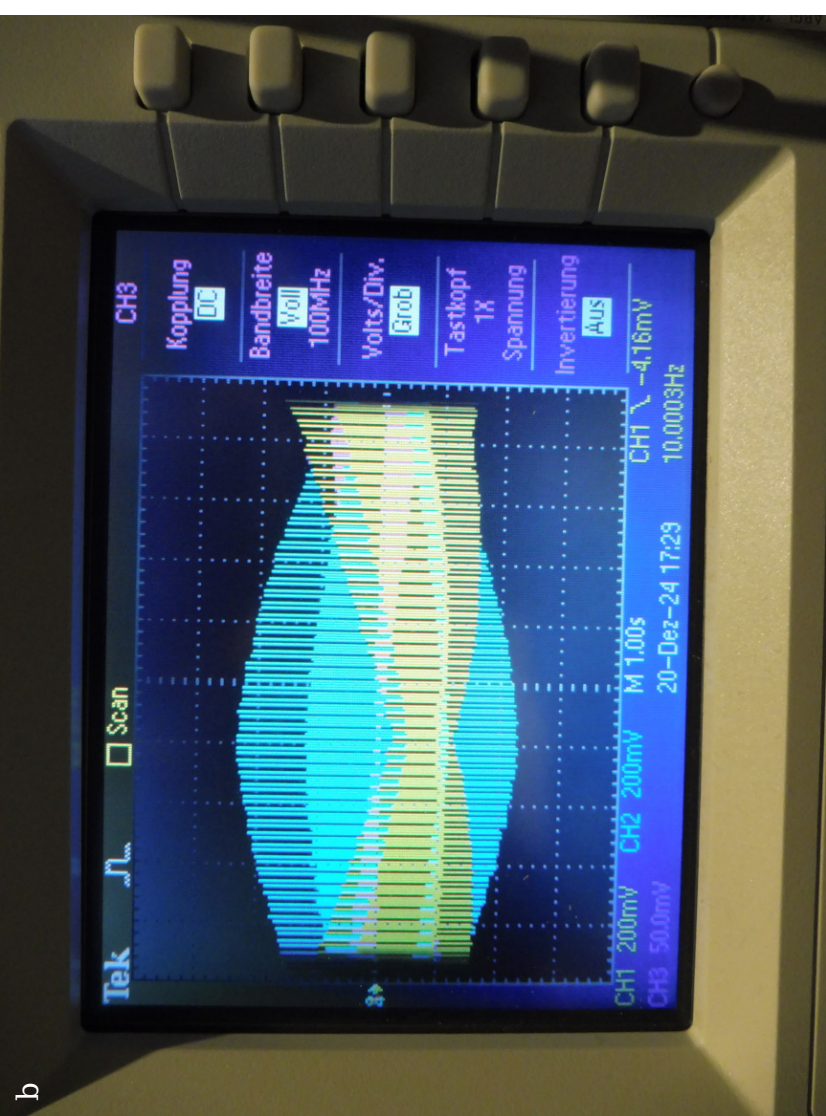
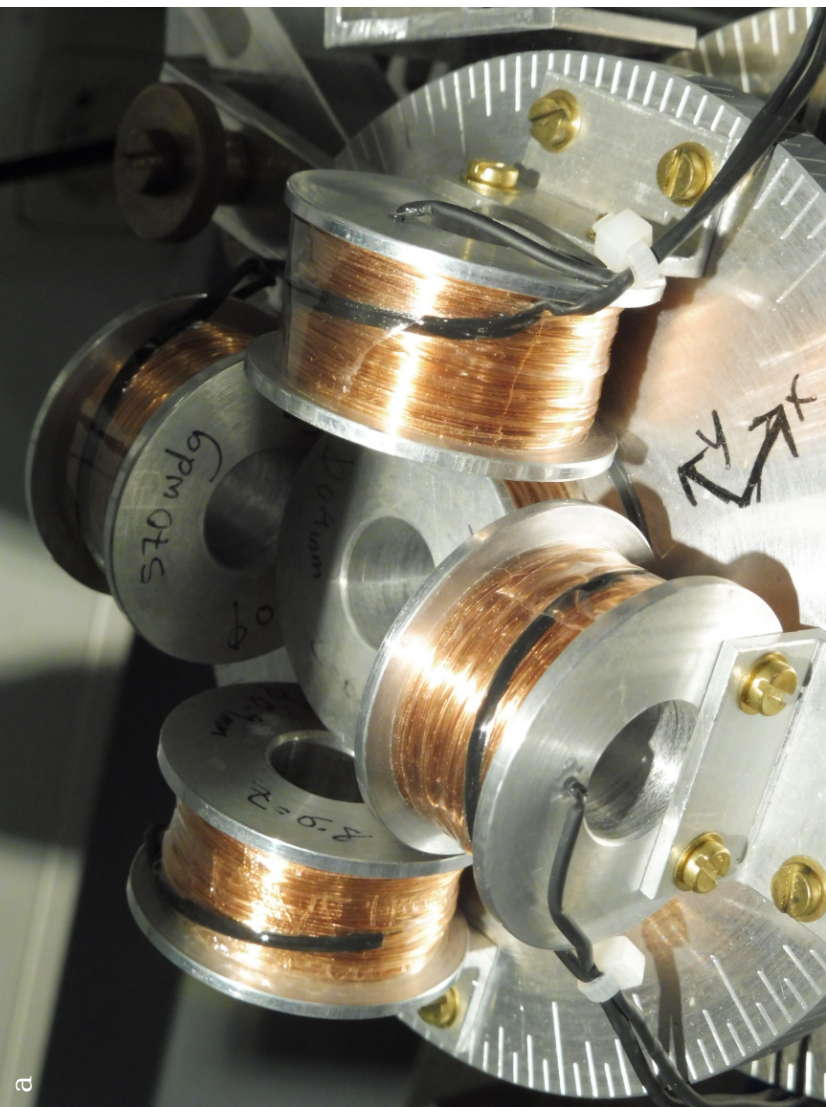


Figure 1 (see page 6): Setup. (a) Coils producing a homogeneous, time-periodic external magnetic field \mathbf{H}_{ext} , driven by a three-channel wave generator connected to three current amplifiers (not shown). The field components in x and y directions are produced by the two upright coil pairs, the z component evolves from the single, flat-lying coil. (b) Current through the coils, displayed by an oscilloscope. It is proportional to the magnetic field component produced by each coil. Details about the time modulation will be given in later sections. (c) Reflection-microscopy image of the used ferromagnetic stripe pattern with paramagnetic particles (top view). The gray stripes are magnetized in $+z$ (out-of-plane) direction, the green stripes are magnetized oppositely. One can see single colloidal particles and bipeds (rods) on top of the pattern. A more detailed description of bipeds can be found in Section 3.1.

2 Background

2.1 Setup

The central part of the setup are the mentioned paramagnetic colloidal particles placed on the ferromagnetic substrate, which is patterned with up and down magnetized stripes (lattice constant $a = 7 \mu\text{m}$, see Figure 1c). The stripes produce a stationary, space-periodic magnetic field \mathbf{H}_p . This *pattern field* is superimposed by a time-periodic, homogeneous *external field* \mathbf{H}_{ext} of modulus 4 kA m^{-1} (Figure 1b). The external field is produced by two coil pairs in x and y direction and a single coil in z direction (Figure 1a), driven by a three-channel wave generator and three current amplifiers.

The particles have diameter $d = 2.8 \mu\text{m}$ and are paramagnetic with an effective magnetic susceptibility $\chi_{\text{eff}} = 0.6$ [6, p. 1664]. They are immersed in demineralized water and their (overdamped) motion is caused by magnetic¹ forces.

A final but important detail is that the substrate is coated with a polymer film (thickness or height $h \approx 1.6 \mu\text{m}$ [4, p. 5055]), on top of which the particles are placed. This implies that the particles always have at least the elevation h above the pattern and so are only feeling a pattern field \mathbf{H}_p that is a “blurred” version of the pattern magnetization; they experience the *universal* pattern field.

This universal field corresponds to the blurred pattern in the sense that, up to a scaling factor, its Fourier series equals that of the magnetization pattern, however truncated to only the leading Fourier components. This holds because the magnetic field is curl-free in the current-free, non-permeable space above the magnetic pattern, and so can be described by a magnetic

¹And sometimes, at sufficiently high velocities, also hydrodynamic.

potential ψ fulfilling the Laplace equation. From the representation of the Laplace equation in Fourier space,

$$((iq_x)^2 + (iq_y)^2 + (iq_z)^2)\psi = 0, \quad (1)$$

together with the fact that q_x and q_y are real due to the periodicity of the pattern, we can conclude $q_z = \pm iq_\perp := \pm i\sqrt{q_x^2 + q_y^2}$. Since the boundary condition $H_p \xrightarrow{z \rightarrow \infty} 0$ is only fulfilled for the case of a pattern field that exponentially decays with the elevation above the pattern, the Fourier coefficients of the exponentially increasing solution vanish completely. As the decay constant of each mode is given by q_\perp , at sufficiently high elevation above the pattern the lowest Fourier mode (for the stripe pattern: $q_\perp = \frac{2\pi}{a}$) will be dominating over all others, and the details of the magnetization pattern become unimportant [4, p. 5046]. So, conversely, only those properties of the pattern which determine the lowest Fourier mode are relevant. For the periodic patterns used in this thesis, the stripe and the square pattern, that are just the symmetry properties of the pattern [4, p. 5067].

2.2 Adiabatic and robust transport

The polymer film simplifies the theoretical treatment of the magnetic forces by the external and pattern magnetic fields: It allows us to calculate the two-dimensional energy landscape in which the particles reside, and which is generated by both fields. The external field is modulated with time so that this potential landscape changes; however, this modulation is slow enough for the particles to stay trapped in their minima and move with them. So the particles follow the minimum positions and don't "march through", i. e. aren't thermally excited across the barrier between two potential wells. This is called an *adiabatic* process. In this way, given the specific pattern, the external magnetic field - if chosen appropriately - *instantaneously* determines the state of the system. It can hence be used to control the particles, and the space where all appropriate external field vectors (that is, the vectors of the homogeneous external magnetic vector fields) live is called *control space* \mathcal{C} . The space where we observe the motion of the colloids is the *action space* \mathcal{A} [4, p. 5046].

Figure 2 illustrates this principle for a one-dimensional case: On the left, the external field is depicted as red arrow. In our experiments the modulus of the external field generally stays constant, and so the control space - the region in which the tip of the red arrow moves - has the form of a circular ring (white/gray/black ring in left part of figure). In this example the control space is one-dimensional and can thus be parametrized by a single *control parameter* s , the same which can also parametrize the path of the arrow tip (line inside the ring). As already indicated in the previous paragraph, the

potential landscape in action space (gray mountains in right part of Figure) changes when the external field changes and so here the minimum position follows a path in action space (gray/green stripe). This path is drawn in the right of Figure 2 and can also be parametrized by the control parameter s . In Figure 2, both for control and action space path the parameter values are symbolized by the changing lightness.

Figure 2, as well as Figure 1c, already suggests that we restrict our investigation to systems that are periodic in space and time, as imposed by the space-periodic, static pattern and the time-periodic, homogeneous external field. Therefore the control and action space trajectories are closed in a reduced zone scheme and we call them *control loop* and *action loop*² [3, p. 3]. Both periodicities again facilitate the theoretical description: As the potential landscape looks the same after one temporal period, the potential minima with their enslaved particles must be in an equivalent position as before, which means the particles have been transported a lattice vector apart or find themselves at the same place again³. Which of these cases holds is, following what we have seen above, completely determined by the control loop.

In the figure the control space has a hole which the control loop winds around, i. e. the control space is not simply connected. This is necessary for transport to occur, as we discuss in the following.

Under the assumption the potential continuously depends on the external field, a *small* deformation of the loop will also cause a small deformation of the particle path and hence also a small deformation of the displacement after completing one control loop period. This displacement after completion of one control loop, on the other hand, must always equal a lattice vector. Now the only possibility of a small displacement which is a lattice vector is a zero displacement. So the particle even has to experience *zero* change under gentle deformations of the loop; the transport is *robust*.

From this it follows that nontrivial transport by a non-zero lattice vector can only happen if the loop *winds* around some hole in control space. Otherwise the loop could continuously be contracted to a point while the displacement being invariant, but a loop contracted to a point means just a static field and hence no transport. Any deformation of the loop that leads to a different displacement thus necessarily is non-continuous; it needs to pull the loop through the hole, and meanwhile eventually an intermediate state must occur where the adiabatic conditions are not fulfilled.

To understand what that means, i. e. what happens in the hole, let's consider a gedankenexperiment of a particle being transported in a minimum by a loop, with the loop being continuously deformed. As long as the par-

²The action loop is closed in the sense that we can describe action space as single unit cell with periodic boundary conditions, see later.

³Which is a special case of the former, with the zero vector as lattice vector.

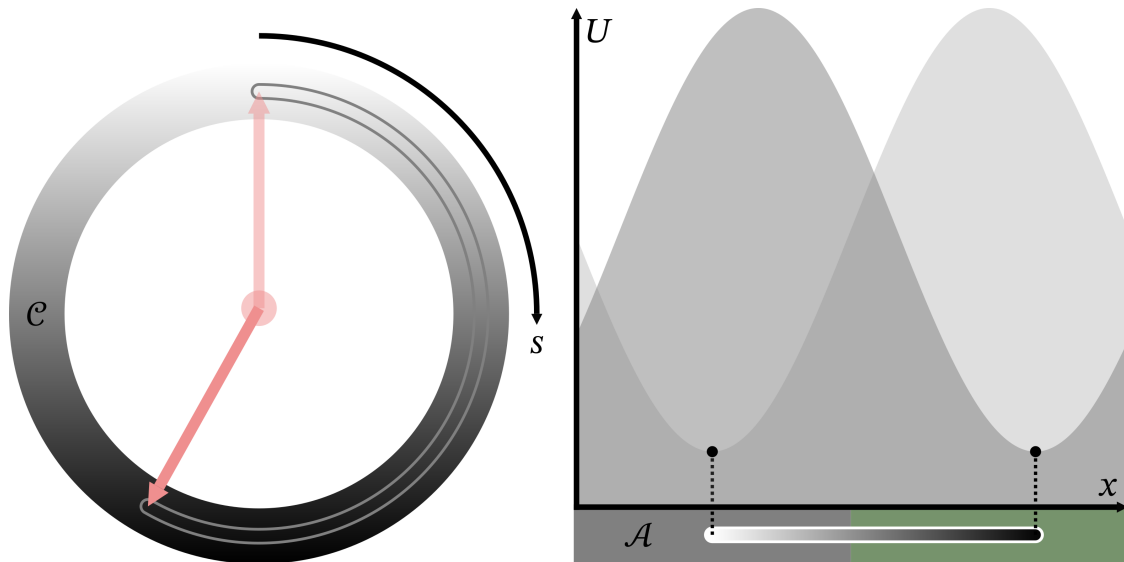


Figure 2: Basic principle of topological transport. In the control space \mathcal{C} (white/gray/black ring in left part) the external magnetic field (red arrow) draws the control loop (curved white/gray/black line). After one period, the control loop will be completed and form a closed path. In the action space \mathcal{A} (gray/green stripe in right part), for each point in control space there is a potential (gray landscape) with (here) one minimum and one maximum. Running the control loop changes the potential so that the minimum moves along the action loop (straight white/gray/black line). After one period, the minimum will have moved one lattice constant; then also the action loop can be considered closed due to the periodicity of the pattern, see Figure 3 below. The lightness modulation of the action and control loops represents their parametrization by the control parameter s . The minimum can enslave a particle (not shown) that follows its position. The control fence is at the hinge (transparent red circle) of the red arrow.

ticle always stays in that named minimum, the displacement after one period will be the same. But now assume we manage to deform the loop into another one yielding a *different* displacement. As the particle won't leave its minimum in the overdamped system, at some point the minimum has to disappear (e.g. by the potential becoming flat in one direction or by the minimum turning into a saddle point). Just this will happen if the control loop crosses⁴ some specific set of points in the holes of control space. Let's call this set *control fence*. In the example from Figure 2, the control fence is at the hinge (transparent red circle) of the red arrow. (Why that is the case we will discuss in Section 3.3.)

2.3 Topological transport

We can get a deeper understanding of this transport process when looking at the *product space* $\mathcal{C} \times \mathcal{A}$ [2, p. 3]. The case shown in Figure 2 - the transport over a one-dimensional pattern (our stripes) by modulation of a single control parameter - assumably is the simplest one to visualize. In this example, both \mathcal{A} and \mathcal{C} are one-dimensional; hence $\mathcal{C} \times \mathcal{A}$ is two-dimensional and is depicted as a rectangle in the left part of Figure 3. However, \mathcal{C} and \mathcal{A} should not really be thought of as stripes. Their ends correspond to the same state (for \mathcal{C}) or to equivalent ones (for \mathcal{A} , being one lattice vector apart) and can thus be joined. Consequently, also opposite sides of the product space rectangle can be joined and $\mathcal{C} \times \mathcal{A}$ becomes a torus (right part of Figure 3).

The points which form the white/gray/black line on this product space torus are the control loop points together with their corresponding action loop points. We will call the set of this points just the *loop*. For completeness we note that in our case, with both \mathcal{C} and \mathcal{A} being one-dimensional, we have no choice where to put the non-trivial loop on the torus. Because, there is only one non-trivial closed control loop, and it already fills the entire control space (just like indicated in the left of Figure 2); and as there is only one minimum per unit cell, it completely determines the corresponding action loop due to the adiabatic condition. Also in the general case there is a subset of the product space where loops can pass through; this subset is the *stationary sub-manifold* for our particles [4, p. 5050]. In Figure 2 the loop covers the whole stationary sub-manifold, but in general the stationary sub-manifold can be bigger than the loop [4, pp. 5052, 5054, 5057].

So if we, as in Figure 3, now plot the loop (or the sub-manifold) on this torus, we see that winding once around in \mathcal{C} we necessarily also loop around once in \mathcal{A} . This is a visualization of the fact that one cycle of the control parameter (e.g. one magnetic moment rotation, walking step or swimming stroke - see later) is *coupled* to a displacement.

For future reference, we introduce two more terms: The *action fence* is

⁴Or approaches, in experiment.

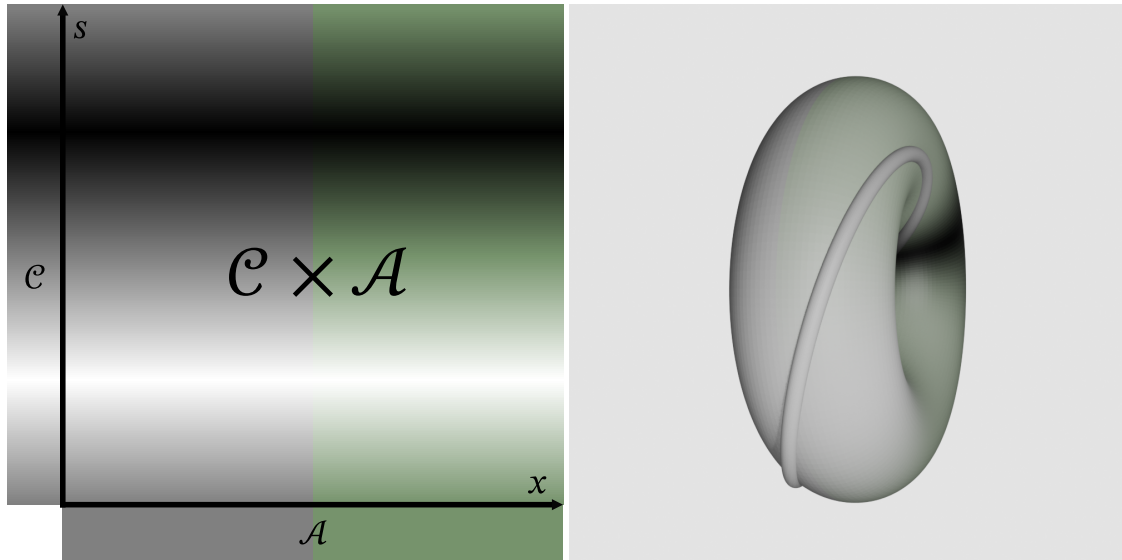


Figure 3: Representation of topological transport in the product space $\mathcal{C} \times \mathcal{A}$. Left: Construction of the product space as cartesian product of the control space \mathcal{C} and the action space \mathcal{A} . The gray or green color represents the position in \mathcal{A} , the lightness stands for the control parameter in \mathcal{C} . Right: Taking into account the periodic boundary conditions for control parameter and action space position, opposite edges of the product space rectangle can be joined to a torus. A plot of the loop in product space (white/gray/black line), here equal to the stationary sub-manifold for our particles, makes visible how one cycle of the control parameter is coupled to a displacement in action space. Figure strongly inspired from Figure 3b in [4, p. 5049].

the set of all points in action space that are stationary while the control loop is crossing the control fence. Finally, the set of pairs of corresponding control fence points and action fence points – living in the holes of $\mathcal{C} \times \mathcal{A}$ – is called just *fence* \mathcal{F} .

We can now rephrase the fact stated above – the fact that if transport occurs, the sub-manifold also winds around action space when it winds around control space. With our new terms, this is equivalent to saying: *If non-trivial transport occurs, the loop winds around a fence*. The inverse statement is also true, which we will look into in Section 3.3. These properties characterize the described transport process to be *topological* [4, p. 5067].

3 Zeroth order, or: how to move

3.1 Shaping and orienting agile bipeds

The main goal of this work was producing colloidal *agile bipeds* – rods like already shown in Figure 1c, but more nimble than in the previous projects thanks to an independent control of their *foothold* and their *orientation*.⁵ As we will see shortly, the former is caused by the (local) substrate–particle interaction whereas the latter arises from the (nonlocal⁶) particle–particle interaction. The possibility to address both independently will provide us with more options to control the movement of colloidal assemblies.

The decoupling of foothold and orientation is achieved by making the external field a superposition of a *low-frequency field* $\mathbf{H}_{\text{LF}}(t)$ and a *high-frequency field* $\mathbf{H}_{\text{HF}}(t)$,

$$\mathbf{H}_{\text{ext}}(t) = \mathbf{H}_{\text{LF}}(t) + \mathbf{H}_{\text{HF}}(t) \quad (2)$$

$$= \tilde{\mathbf{H}}_{\text{LF}}(t) + \tilde{\mathbf{H}}_{\text{HF}}(t) \cos(\omega_{\text{HF}}t) \quad (3)$$

where the directions of both amplitudes $\tilde{\mathbf{H}}_{\text{LF}}(t)$ and $\tilde{\mathbf{H}}_{\text{HF}}(t)$ are modulated adiabatically. This means their directions are changed periodically with a period $T = 20$ s, which is much longer than the oscillation period $T_{\text{HF}} = \frac{2\pi}{\omega_{\text{HF}}} = 0.1$ s of the high-frequency field $\mathbf{H}_{\text{HF}}(t)$. Also, the low-frequency amplitude is chosen significantly weaker than the high-frequency field amplitude, $\tilde{H}_{\text{LF}} = 0.3\tilde{H}_{\text{HF}}$. With these properties,

- the high-frequency field $\mathbf{H}_{\text{HF}}(t) = \tilde{\mathbf{H}}_{\text{HF}}(t) \cos(\omega_{\text{HF}}t)$ is oscillating too fast for the colloid displacement to follow the oscillation, and

⁵On an abstract level, “coupling” here means something similar as in the previous section: The change of one quantity implies the change of the other. In the previous section this was the case (between control parameter and displacement), here it isn’t (between foothold and orientation).

⁶Strictly, this interaction only *appears* nonlocal in our description of the system.

- the low-frequency field $\mathbf{H}_{\text{LF}}(t) = \tilde{\mathbf{H}}_{\text{LF}}(t)$ is so weak that the high-frequency field is dominating over it.

Before justifying these assumptions let's look what they imply: The strong high-frequency field dominates the magnetic particle-particle interactions by magnetizing the particles and inducing dipolar attractions between them. The oscillation does not matter in this case because at any time the particles are all magnetized in the same direction. Therefore the particles form rods - our bipeds from Figure 1c - the direction of which is locked to that of the high-frequency field amplitude $\tilde{\mathbf{H}}_{\text{HF}}(t)$.

Although the high-frequency field dominates the particle magnetization, due to its oscillation it does not contribute to the time-averaged magnetization. That quantity is then completely determined by the low-frequency field; the direction of the time-averaged magnetization and magnetic moment is locked to that of the low-frequency field $\mathbf{H}_{\text{LF}}(t)$.⁷ We also elaborate on the time averaging later, but already from now we only consider the time-averaged magnetic moment and refer to it just as *the* magnetic moment.

We describe this as sketched in Figure 4: Each of the field $\mathbf{H}_{\text{LF}}(t)$ and the amplitude $\tilde{\mathbf{H}}_{\text{HF}}(t)$ lives in its own control space - the *low-frequency control space* \mathcal{C}_{LF} or the *high-frequency control space* \mathcal{C}_{HF} , respectively (top left and top right).

The high-frequency field amplitude controls the biped orientation: For a biped consisting of n single particles each with diameter d , the *biped vector* \mathbf{b}_n , pointing from one end of the biped to the other (center of Figure 4), is always parallel to the vector $\tilde{\mathbf{H}}_{\text{HF}}$. The length $b_n := nd$ of the biped vector equals the actual length of the rod. In this way, for a rod of given length, the vector $\tilde{\mathbf{H}}_{\text{HF}}$ can be transcribed into a vector \mathbf{b}_n in the vector space of all possible biped vectors \mathbf{b} . We call this vectorspace the *high-frequency transcription space* \mathcal{T}_{HF} (bottom right). This \mathbf{b}_n vector dictates the biped orientation (center).

In an analogous manner, the biped magnetic moment $\mathbf{m}_n := nV\chi_{\text{eff}}\mathbf{H}_{\text{LF}}$ is locked parallel to the low-frequency field while its modulus is proportional to the rod length (center). Thus also $\tilde{\mathbf{H}}_{\text{LF}}$ can be transcribed into a vector \mathbf{m}_n in the vector space of all possible biped magnetic moments \mathbf{m} . Let's name this vector space the *low-frequency transcription space* \mathcal{T}_{LF} (bottom left). The \mathbf{m}_n vector dictates the biped magnetic moment (center).

In the next two sections, we will deepen our understanding of the relation between control, transcription and action spaces by theoretically looking at particular examples how to make agile bipeds move.

⁷We won't talk about the low-frequency amplitude $\tilde{\mathbf{H}}_{\text{LF}}$ any more, as it just equals \mathbf{H}_{LF} .

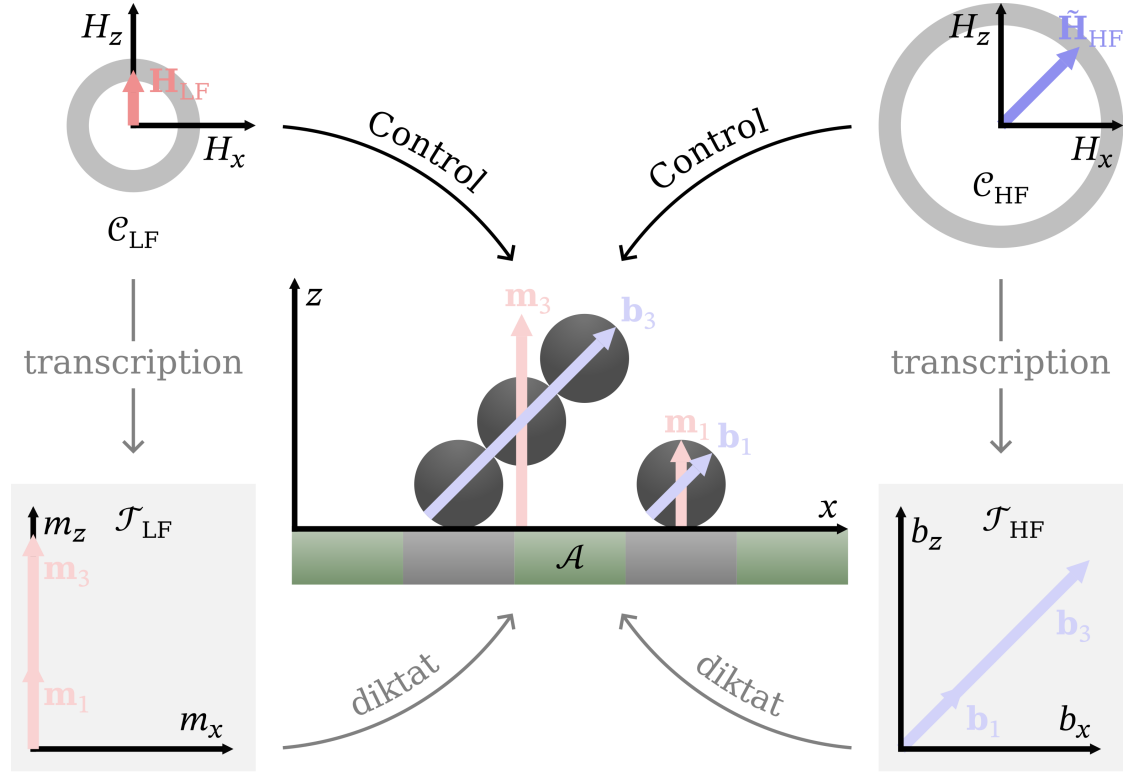


Figure 4: Relations between control spaces, transcription spaces and action space. The low-frequency magnetic field \mathbf{H}_{LF} and the high-frequency magnetic field amplitude $\tilde{\mathbf{H}}_{\text{HF}}$, living in the low- and high-frequency control spaces \mathcal{C}_{LF} and \mathcal{C}_{HF} , can be transcribed into the magnetic moments \mathbf{m} and the biped vectors \mathbf{b} of the agile bipeds. These are elements of the low-frequency and high-frequency transcription spaces \mathcal{T}_{LF} and \mathcal{T}_{HF} ; their moduli are proportional to the biped length. These vectors are dictated to the bipeds in the action space \mathcal{A} . So in total, the control of the biped orientation and adherence can be seen as a composition of transcription and diktat.

3.2 Simulations: sliding and walking

As a reminder: The high-frequency field amplitude $\tilde{\mathbf{H}}_{\text{HF}}$ controls the biped orientation and the low-frequency field \mathbf{H}_{LF} the magnetic moment. The direction of each $\mathbf{H}_{\text{LF}}(t)$ and $\tilde{\mathbf{H}}_{\text{HF}}(t)$ can be changed independently, while keeping the moduli constant.

The effects of these modulations are illustrated with simulation results from the Brownian dynamics software developed by Adrian Ernst [2]. The simulation parameters were chosen corresponding to the experimental parameters as given in Section 3.4, while the biped orientation was locked to the $\tilde{\mathbf{H}}_{\text{HF}}$ direction by constraint. Figures 5 and 6 show the simulated results, that is, the effects of separately modulating one of \mathbf{H}_{LF} and $\tilde{\mathbf{H}}_{\text{HF}}$ while keeping the other one fixed. Snapshots of these vectors (red and blue arrows) are shown in first column, where they draw their control loops (white/gray/black lines) in their control spaces (transparent gray spheres).⁸ The second column contains snapshots of a simulated 3-particle biped in action space, and in the third and fourth column we see the \mathbf{m}_3 (red arrow) and \mathbf{b}_3 (blue arrow) vectors in their transcription spaces. Also, here not only the vectors but also the control loops are transcribed to the transcription spaces (white/green/black lines).

Let us focus on Figure 5 first. There the biped magnetic moment is modulated by adiabatically rotating \mathbf{H}_{LF} counter-clockwise. At the same time, $\tilde{\mathbf{H}}_{\text{HF}}$ and thus the biped orientation is kept fixed and parallel to the stripes of the pattern. We see that, in this situation, the biped lays flat on the ground along the stripes and transversally *slides*; its *foothold* on the substrate is modulated. After completion of the loop, it has moved one lattice constant to the left.

In Figure 6, the biped orientation is modulated by driving a control loop with $\tilde{\mathbf{H}}_{\text{HF}}$. Now \mathbf{H}_{LF} is kept fixed, namely upwards perpendicular to the pattern. Now we see the biped *walk*: Its grounded end, or grounded *foot*, always seems to be fixed on the substrate, more precisely on a gray stripe. But at two times (here $t = 0.25T$ and $0.75T$) the biped switches its grounded foot. At the first time it also gains foothold on a different stripe, and it stays there afterwards. In this way, after completion of the loop the biped has moved one lattice constant to the right.

3.3 Rolling wheel rule

In the simulations just shown the sliding loop was driven counter-clockwise and moved the biped to the left, while the walking loop ran clockwise and induced transport to the right. This is the same behavior which a wheel rolling on the ground shows: When it is rotating (counter-)clockwise, it rolls

⁸As we now take into account all three x , y and z directions the control spaces are spheres (in Figure 4 they were circles as we were only considering the x and z directions).

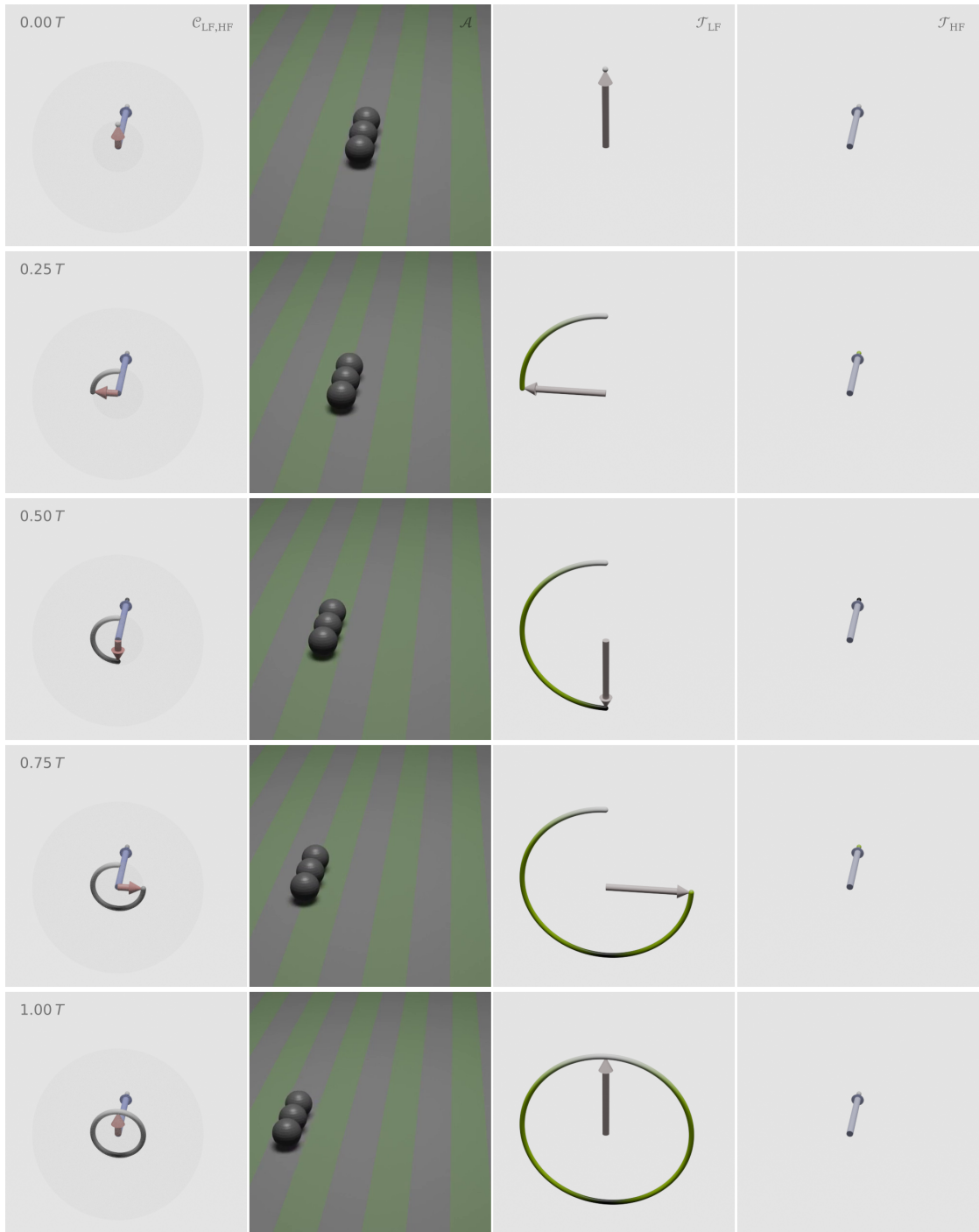


Figure 5: Brownian dynamics simulation results of a biped sliding due to direction modulation of the low-frequency field \mathbf{H}_{LF} . The snapshots are taken from Video 1 (accessible via the QR code) in intervals of $0.25T$, where $T = 20$ s is the period of the adiabatic modulation of the amplitude. The columns (from left to right) show the control spaces, the action space, the low-frequency and the high-frequency transcription space.





Figure 6: Brownian dynamics simulation results of a biped walking due to direction modulation of the high-frequency field amplitude $\hat{\mathbf{H}}_{\text{HF}}$. The snapshots are taken from Video 2 (accessible via the QR code) in intervals of $0.25T$, where $T = 20$ s is the period of the adiabatic modulation of the amplitude (*not* the period of the high-frequency oscillation). The columns show the same spaces as in Figure 5.



to the right (left). This is the *rolling wheel rule*, as discovered in my group and formulated in [1, p. 6].

For the walking motion of bipeds the reason for its validity is the same: Both the lowest point of a wheel and the footpoint of the biped are fixed to the ground so that only the upper part can move (see Figure 7, right part).

For the sliding motion of the colloidal particles the reason is a bit different. We can understand the motion by recognizing that the particle magnetic energy is minimal at the places where its magnetic moment is parallel to the pattern field \mathbf{H}_p . As the magnetic moment is itself aligned with the low-frequency field \mathbf{H}_{LF} , adiabatic rotation of the latter leads to transport. The direction is determined by the shape of the pattern field (Figure 7, left part).⁹

Please keep in mind that for the above argument just given and illustrated in the left part of Figure 7 we have made no assumption about the modulus of \mathbf{H}_{HF} . We can therefore conclude that here adiabatic non-trivial transport indeed always occurs when the control loop winds around the hinge of the red arrow. This is the justification why the low-frequency control fence looks as in Figure 2.

I hope it has become intuitively clear by now how the sliding and walking motion are supposed to work. To justify the thoughts theoretically, and to be able to quantitatively predict the effect of arbitrary control loops, we need to derive expressions for the potential and the fence. This is what we do in the next two sections.

3.4 Calculation of the potential

We describe our system as the magnetic pattern, generating a stationary, space-dependent magnetic field \mathbf{H}_p , on which N of our paramagnetic particles are placed arbitrarily. In addition, the homogeneous, time-dependent external magnetic field \mathbf{H}_{ext} is applied.

As the system is overdamped, its time evolution in the adiabatic case is determined by a potential

$$U(\mathbf{R}) = U_{sp}(\mathbf{R}) + U_{pp}(\mathbf{R}). \quad (4)$$

Here $\mathbf{R} = (\mathbf{r}_1, \dots, \mathbf{r}_N)$ is the $3N$ -dimensional vector of all N particle positions; U_{sp} is the energy by the magnetic substrate-particle interactions and U_{pp} is the energy from the magnetic particle-particle interactions.

We first look at the substrate-particle interaction energy: Each single particle (diameter $d = 2.8 \mu\text{m}$, volume $V = \frac{4\pi}{3} \left(\frac{d}{2}\right)^3$, effective magnetic susceptibility $\chi_{eff} = 0.6$) is magnetized by the total magnetic field $\mathbf{H} = \mathbf{H}_p + \mathbf{H}_{ext}$, and

⁹As a side note: If we imagine the field lines of \mathbf{H}_p above the pattern, they are curved towards the ground – just as the top half of a rolling wheel. This can be seen as a deeper reason why the rolling wheel rule is applicable to the sliding motion.

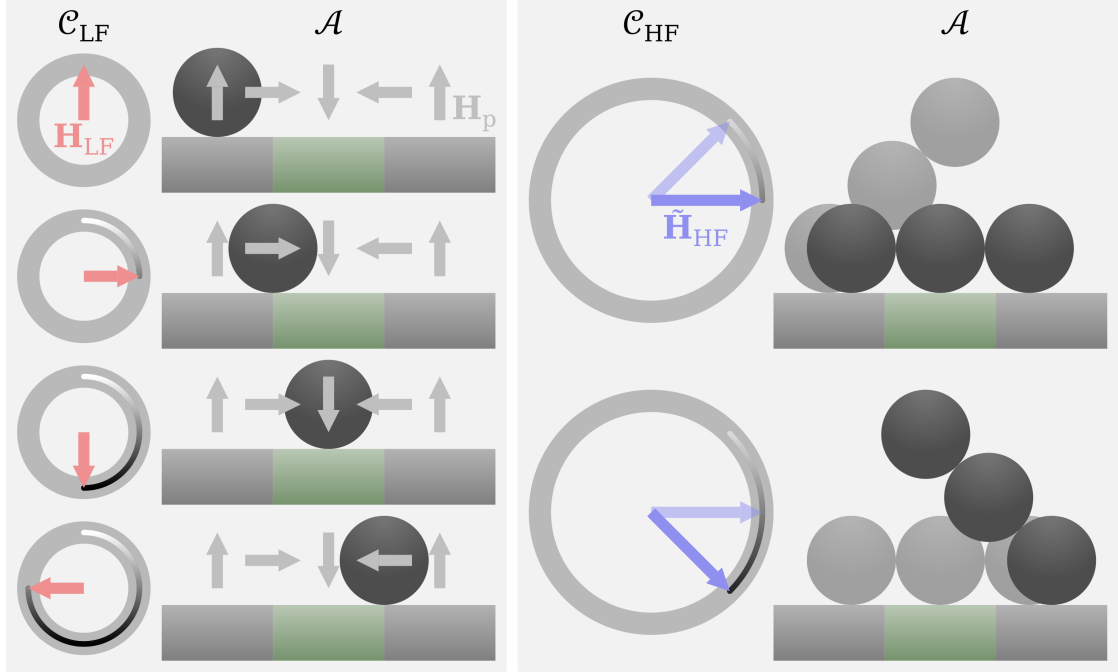


Figure 7: Transport directions induced by low-frequency and high-frequency control loops. Left: Single particles have their potential minimum at the places where the pattern field \mathbf{H}_p is parallel to their magnetic moment, which is itself parallel to the low-frequency field \mathbf{H}_{LF} . Thus a full clockwise adiabatic rotation of \mathbf{H}_{LF} transports the particle one lattice constant to the right (snapshots from top to bottom). The same principle applies for assemblies of particles. Right: Bipedes rotate synchronously with the adiabatically driven high-frequency field amplitude $\tilde{\mathbf{H}}_{HF}$. As already seen in Figure 6, the grounded foot stays roughly fixed but can be switched. Also here, a clockwise rotation of $\tilde{\mathbf{H}}_{HF}$ induces transport to the right.

so gets a magnetic moment $\mathbf{m} = V\chi_{\text{eff}}\mathbf{H}$. Therefore in the total field it has the magnetic energy $U_i = -\mu_0\mathbf{m} \cdot \mathbf{H} = -\mu_0V\chi_{\text{eff}}\mathbf{H}^2$.

In the scalar product we can now abandon (“gauge away”) the spatially constant $\mathbf{H}_{\text{ext}}^2$ term, and neglect the \mathbf{H}_p^2 term because $H_p \approx 5 \text{ A m}^{-1}$ is much smaller than $H_{\text{ext}} = 4 \text{ kA m}^{-1}$ [4, p. 5046].¹⁰ So $U_i \approx -2\mu_0V\chi_{\text{eff}}\mathbf{H}_p \cdot \mathbf{H}_{\text{ext}}(t)$ and the total particle–substrate interaction energy $U_{\text{sp}} = \sum_{i=1}^N U_i$ reads

$$U_{\text{sp}}(\mathbf{R}(t)) = -2\mu_0V\chi_{\text{eff}} \sum_{i=1}^N \mathbf{H}_p(\mathbf{r}_i(t)) \cdot \mathbf{H}_{\text{ext}}(t). \quad (5)$$

Let us now consider the time averaging. In our overdamped system the magnetic force is always compensated by the friction, so the equation of motion for a single particle, not interacting with other particles, reads

$$6\pi\eta\frac{d}{2}\mathbf{r}_i(t) = \mu_0\chi_{\text{eff}}V\nabla(2\mathbf{H}_p \cdot \mathbf{H}_{\text{ext}}(t)), \quad (6)$$

or in the frequency domain,

$$6\pi\eta\frac{d}{2} \cdot (-i\omega)\mathbf{r}_i(\omega) = \mu_0\chi_{\text{eff}}V\nabla(2\mathbf{H}_p \cdot \mathbf{H}_{\text{ext}}(\omega)). \quad (7)$$

To find the characteristic angular frequency ω_c above which the particles stop being able to follow, let’s demand $|\mathbf{r}_i(\omega_c)| \stackrel{!}{=} d$. This means upon oscillation the particle is being displaced by its own diameter. Then the strength of the friction is $|6\pi\eta\frac{d}{2} \cdot (-i\omega_c)\mathbf{r}_i| = 3\pi\eta d^2\omega_c$. On the other hand, for the magnetic force we estimate $|\mu_0\chi_{\text{eff}}V\nabla(2\mathbf{H}_p \cdot \mathbf{H}_{\text{ext}})| \approx \mu_0\chi_{\text{eff}}\frac{4\pi}{3}\left(\frac{d}{2}\right)^3 \cdot \frac{1}{a}2H_pH_{\text{ext}} = \frac{\pi}{3}\frac{d}{a}\mu_0\chi_{\text{eff}}d^2H_pH_{\text{ext}}$. Setting these equal, we get the condition

$$\text{Mn} := \frac{\eta\omega_c}{\mu_0\chi_{\text{eff}}H_pH_{\text{ext}}} \stackrel{!}{=} \frac{d}{9a} \approx 0.04. \quad (8)$$

The number Mn is called *Mason number* [6, p. 1669].¹¹ Plugging in all parameters as given above and solving for the characteristic angular frequency yields $\omega_c \approx 0.6 \text{ s}^{-1}$. This result confirms the experimental observation that the particles can follow the adiabatic field modulation with $\omega = \frac{2\pi}{T} = \frac{2\pi}{20\text{s}} \approx$

¹⁰The modulus of the stripe pattern field on top of the polymer film (see Section 2) is $H_p^{(0)} = M_s \frac{2\pi}{a} e \cdot \exp(-\frac{2\pi}{a}h) \approx 5 \text{ A m}^{-1}$. Here $M_s = 6.5 \text{ kA m}^{-1}$ is the effective saturation magnetization of the magnetic pattern, $e = 3.5 \text{ nm}$ its thickness or extension, $a = 7 \mu\text{m}$ the lattice constant and $h = 1.6 \mu\text{m}$ the height of the polymer film [4, pp. 5055, 5073].

¹¹The Mason number is proportional to the viscous/magnetic force ratio. As the former scales with the surface and the latter with the volume, for a biped of length b the Mason number must be multiplied by a factor $\left(\frac{b}{a/2}\right)^{3/2}$ [6, p. 1669].

0.3 s^{-1} but not the high-frequency oscillation with $\omega = \omega_{\text{HF}} = 2\pi \cdot 10 \text{ Hz} \approx 60 \text{ s}^{-1}$.

Therefore instead of the fully time-resolved potential $U(\mathbf{R}(t))$ we can describe the motion of the particle with the potential $\langle U(\mathbf{R}(t)) \rangle$ averaged over a timescale $\frac{2\pi}{6 \text{ s}^{-1}} \approx 1 \text{ s}$. In the experiments $\mathbf{H}_{\text{LF}}(t)$ and $\tilde{\mathbf{H}}_{\text{HF}}(t)$ are not changing significantly at the timescale over which we average, so they can be pulled out of the $\langle \text{angular brackets} \rangle$. From this follows $\langle \tilde{\mathbf{H}}_{\text{HF}}(t) \cos(\omega_{\text{HF}} t) \rangle = \tilde{\mathbf{H}}_{\text{HF}}(t) \langle \cos(\omega_{\text{HF}} t) \rangle = 0$, and so the time-averaged substrate-particle interaction potential is given by

$$\langle U_{\text{sp}}(t) \rangle = -2\mu_0 V \chi_{\text{eff}} \sum_{i=1}^N \langle \mathbf{H}_{\text{p}}(\mathbf{r}_i) \cdot \mathbf{H}_{\text{ext}}(t) \rangle = -2\mu_0 V \chi_{\text{eff}} \sum_{i=1}^N \mathbf{H}_{\text{p}}(\mathbf{r}_i) \cdot \mathbf{H}_{\text{LF}}(t). \quad (9)$$

This expression doesn't contain $\tilde{\mathbf{H}}_{\text{HF}}$, reflecting the fact that the high-frequency field causes no average magnetization of the particles on the considered timescale.

The overall particle-particle interaction potential is the sum of all pair's dipolar interaction energies, $U_{\text{pp}} = \sum_{(i,j)} U_{ij}$, with

$$\langle U_{ij}(\mathbf{R}(t)) \rangle = -\frac{\mu_0}{4\pi} \frac{3\hat{\mathbf{r}}_{ij}\hat{\mathbf{r}}_{ij} - \mathbb{1}}{r_{ij}^3} V^2 \chi_{\text{eff}}^2 \cdot \langle \mathbf{H}_{\text{ext}}(t) \mathbf{H}_{\text{ext}}(t) \rangle \quad (10)$$

$$\approx -\frac{\mu_0}{4\pi} \frac{3\hat{\mathbf{r}}_{ij}\hat{\mathbf{r}}_{ij} - \mathbb{1}}{r_{ij}^3} V^2 \chi_{\text{eff}}^2 \cdot \frac{1}{2} \tilde{\mathbf{H}}_{\text{HF}}(t) \tilde{\mathbf{H}}_{\text{HF}}(t), \quad (11)$$

where $\mathbf{r}_{ij} = \mathbf{r}_j - \mathbf{r}_i$ is the vector between the two particles. The $\mathbf{H}_{\text{LF}} \mathbf{H}_{\text{LF}}$ term is neglected because its norm is much smaller than that of $\tilde{\mathbf{H}}_{\text{HF}} \tilde{\mathbf{H}}_{\text{HF}}$ (by a factor $0.3^2 = 0.09$ in the present experiments). The factor $\frac{1}{2}$ is the value of the $\langle \cos(\omega_{\text{HF}} t) \cos(\omega_{\text{HF}} t) \rangle$ term.

In the following calculation of the fence we will only consider a single particle or biped and not take into account division or merging events, because in the experiments they happen less frequently than the walking or sliding steps. This means the time-averaged dipolar particle-particle interaction potential $\langle U_{ij}(\mathbf{R}(t)) \rangle$ is constant and we just use the substrate-particle interaction potential from Equation (9). The particle-particle interaction is then accounted for by assuming that the bipeds are rigid and aligned along $\tilde{\mathbf{H}}_{\text{HF}}$.

3.5 Theory: Control fence for the stripe pattern

3.5.1 Result and heuristical argument

In the simulation we have already seen a sliding motion (by keeping fixed the high-frequency field amplitude, $\tilde{\mathbf{H}}_{\text{HF}}$, and therefore also the rod direction) and a walking motion (by keeping the adiabatic low-frequency field \mathbf{H}_{LF} fixed, and with it the biped magnetic moment).

A quantitative understanding of these processes is delivered by the fence which we will calculate in the next section. In fact, we will do this not in the control spaces but directly in the transcription spaces \mathcal{T}_{LF} and \mathcal{T}_{HF} . An advantage of them over the control spaces is that they allow to simultaneously represent the behavior of rods with different lengths.

Before, we will already look at the results and make them plausible.¹² My theory presented in the next section predicts that bipeds with any fixed direction slide with the same velocity as its constituent particles would, if they were separated. This is plausible because a modulation of the low-frequency field just shifts the potential and so all particles of the assembly are transported in the same way. Therefore the low-frequency control fence looks the same as for single particles, i. e. as in Figure 2 on page 10, but extended in y direction. This is depicted in Figure 8.

On the other hand, the calculation will show that the fence in the high-frequency transcription space \mathcal{T}_{HF} consists of straight lines in y direction at non-zero multiples of the lattice constant a , see Figure 9. This is plausible too: A biped can step one stripe further if it (more precisely: its projection on the x axis) is more than one lattice constant long. If it is shorter, it slides *back* while it switches foot because it can't overcome the potential maximum with its lifted end (see Figure 10, top left). Then it won't reach the next stripe with the other foot. On the other hand, if it is longer, it slides *forward* and steps on the next stripe (Figure 10, bottom left). The distinction in the high-frequency transcription space is that in the second case the transcribed control loop cuts the $b_z = 0$ plane on the right of the line $b_x = a$, whereas in the first case it cuts it on its left.¹³ This holds for any fixed orientation of the low-frequency field, because changing it will just shift the position of the minima. An analogous argument applies for steps of more lattice constants, which makes plausible that the high-frequency control fence looks like in Figure 9.

Having seen the results we now look into the calculation of the fence.

¹²In fact, the calculation was done first and the heuristic arguments were formulated afterwards.

¹³This might not be obvious to you if you are thinking about bipeds for the first time. In this case I suggest you to visualize for yourself how each of the two bipeds moves in \mathcal{A} , and how each of its \mathbf{b} vectors moves in \mathcal{T}_{HF} . For this purpose e.g. two pencils of different lengths can be helpful.

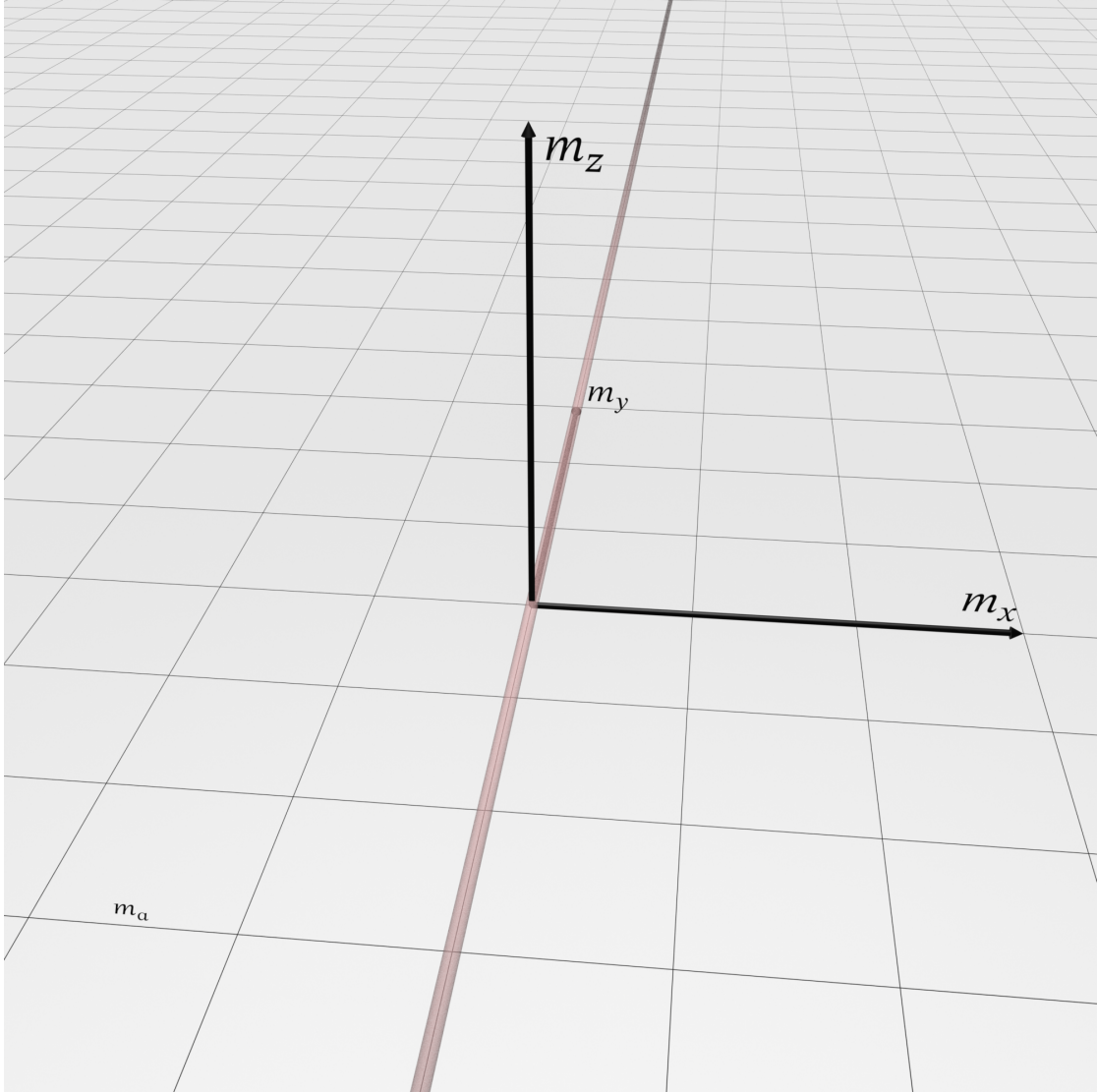


Figure 8: Low-frequency control fence (red line) in the low-frequency transcription space \mathcal{T}_{LF} , as calculated in Section 3.5.2. Here $m_{x,y,z}$ are the x , y and z components of the biped magnetic moment \mathbf{m} , and $m_a := \frac{m_n}{b_n} a$ is the magnetic moment of a biped with length a (the lattice constant of the stripe pattern).

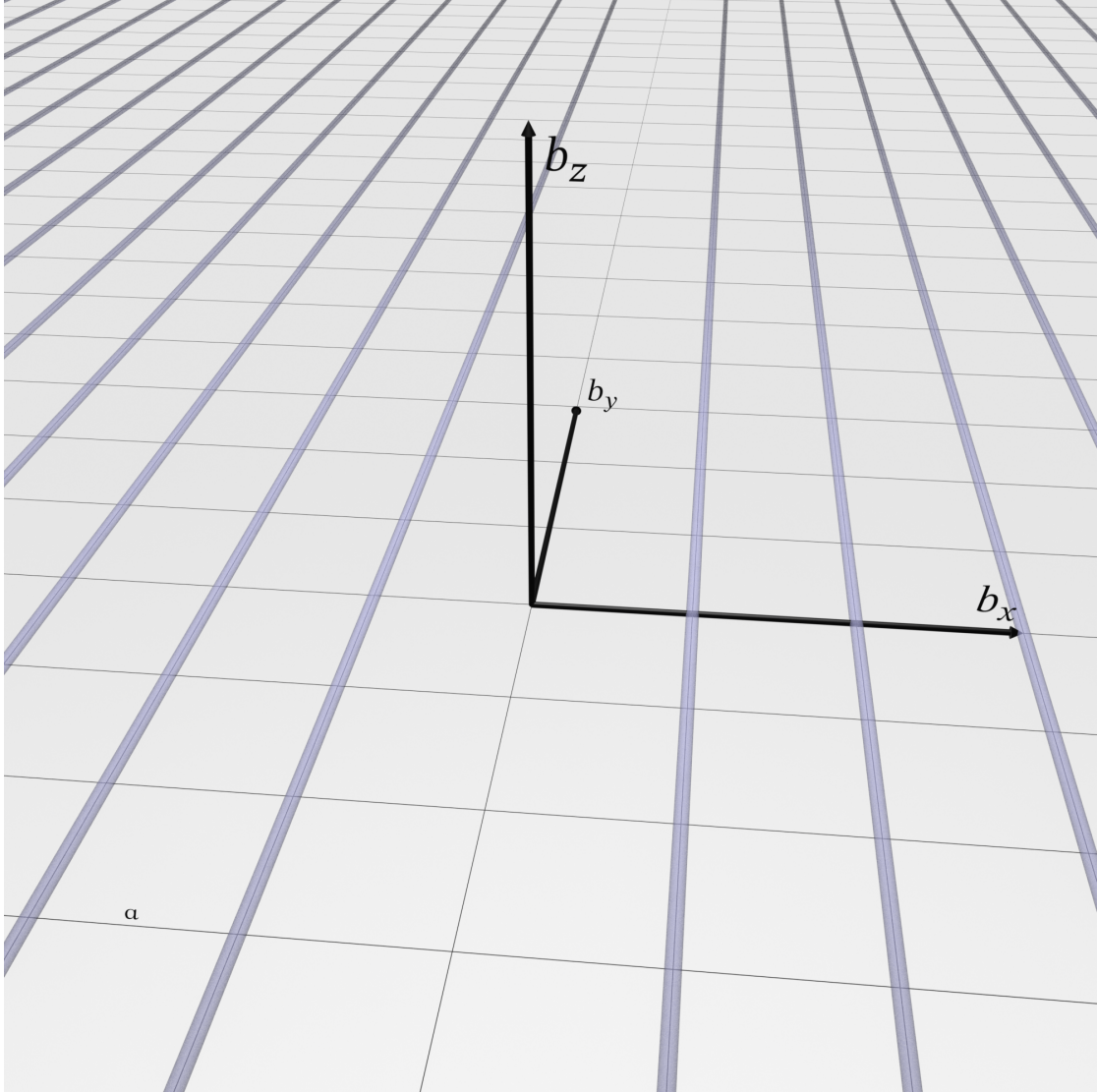


Figure 9: High-frequency control fence (blue lines) in the high-frequency transcription space \mathcal{T}_{HF} , as calculated in Section 3.5.2. Here $b_{x,y,z}$ are the x , y and z components of the biped vector \mathbf{b} , and a is the lattice constant of the stripe pattern.

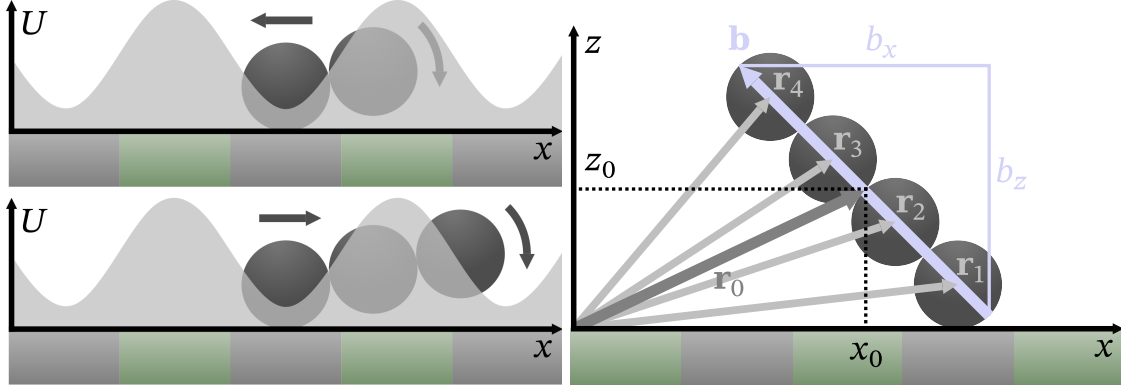


Figure 10: Visualizations for fence determination. Left: Heuristical explanation for high-frequency fence. While stepping down with the lifted foot, the rod slides to the left or the right. Which direction it is determines the standpoint after switching foot and depends of the length: The biped slides into the nearest stationary, symmetric position of minimal energy (see Figure 7). Right: Definition of quantities for the fence calculation. The vectors $\mathbf{r}_{1,\dots,4}$ give the single particles' positions, $\mathbf{r}_0 := (x_0, y_0, z_0)$ is the center position of the rod. The vector \mathbf{b} is the previously introduced biped vector, b_x and b_z are its x and z components.

3.5.2 Derivation

Analogously to Section 2.2, the transcribed control fence is the transcription space region where extrema of the potential U in action space disappear. Thus the conditions for each control fence point are that it

1. renders at least one action space point stationary but
2. non-extremal,

which necessarily means

$$\frac{\partial U}{\partial \left(\frac{2\pi}{a}x_0\right)} \stackrel{!}{=} 0 \quad (12)$$

and

$$\frac{\partial^2 U}{\partial \left(\frac{2\pi}{a}x_0\right)^2} \stackrel{!}{=} 0. \quad (13)$$

These conditions will allow us to calculate the fence. We start with writing out an expression for U , using the coordinates as depicted in the right of Figure 10.

The leading Fourier components of the magnetostatic potential of the stripe pattern just give a cosine function, and the pattern magnetic field \mathbf{H}_p at po-

sition $\mathbf{r} = (x, y, z)$ equals [4, p. 5048]

$$\mathbf{H}_p(\mathbf{r}) = H_p^{(0)} \begin{pmatrix} \sin\left(\frac{2\pi}{a}x\right) \\ 0 \\ \cos\left(\frac{2\pi}{a}x\right) \end{pmatrix} e^{-\frac{2\pi}{a}z} \quad (14)$$

with $H_p^{(0)}$ the modulus of the pattern field at the substrate surface $z = 0$. As announced before, we assume the considered particles are already assembled to one biped and stay so for all times. So the particle-particle interaction potential is constant in time, and the potential of the biped, using Equation (9), is given by

$$U = -2\mu_0 V \chi_{\text{eff}} \sum_{i=1}^N \mathbf{H}_p(\mathbf{r}_i) \cdot \mathbf{H}_{\text{LF}} \quad (15)$$

$$\approx -2\mu_0 V \chi_{\text{eff}} \mathbf{H}_{\text{LF}} \cdot \int_{-b/2}^{b/2} \frac{db'}{d} \mathbf{H}_p(\mathbf{r}_0 + \mathbf{b}') \quad (16)$$

$$= -\frac{2\mu_0 d}{b} \mathbf{m} \cdot \int_{-b/2}^{b/2} \frac{db'}{d} \mathbf{H}_p(\mathbf{r}_0 + \mathbf{b}'). \quad (17)$$

Here, the vectors $\mathbf{r}_{1,\dots,n}$ give the single particles' positions (see Figure 10) and $\mathbf{r}_0 := (x_0, y_0, z_0) := \frac{1}{n} \sum_{i=1}^n \mathbf{r}_i$ is the center position of the rod. As before, d is the diameter of a single colloidal particle, and $\mathbf{m} = \frac{b}{d} V \chi_{\text{eff}} \mathbf{H}_{\text{LF}}$ is the biped magnetic moment. Plugging in Equation (14), we get

$$U = -2\mu_0 H_p^{(0)} \begin{pmatrix} m_x \\ m_y \\ m_z \end{pmatrix} \cdot \int_{-b/2}^{b/2} \frac{db'}{b} \begin{pmatrix} \sin\left(\frac{2\pi}{a}(x_0 + b'_x)\right) \\ 0 \\ \cos\left(\frac{2\pi}{a}(x_0 + b'_x)\right) \end{pmatrix} e^{-\frac{2\pi}{a}(z_0 + b'_z)} \quad (18)$$

with $b'_{x,z} := b' \frac{b_{x,z}}{b}$. Here, b is the length of the biped and $b_{x,z}$ are its x and z projections (see Figure 10); b' parametrizes the position along the biped axis, and analogously $b'_{x,z}$ are its x and z projections.

Rewriting the scalar product $(\alpha, \beta) \cdot (\gamma, \delta) = \alpha\gamma + \beta\delta = \text{Re}((\alpha - i\beta)(\gamma + i\delta))$ this can equally be expressed as

$$\frac{U}{2\mu_0 H_p^{(0)}} = -\operatorname{Re} \left((m_z - im_x) \cdot \int_{-b/2}^{b/2} \frac{db'}{b} e^{i\frac{2\pi}{a}(x_0+b'_x+iz_0+ib'_z)} \right) \quad (19)$$

$$= -\operatorname{Re} \left((m_z - im_x) \cdot e^{i\frac{2\pi}{a}(x_0+iz_0)} \int_{-b/2}^{b/2} \frac{db'}{b} e^{i\frac{2\pi}{a}(b'_x+ib'_z)} \right) \quad (20)$$

$$= -\operatorname{Re} \left((m_z - im_x) \cdot e^{i\frac{2\pi}{a}(x_0+i\frac{b_z}{2})} \int_{-b/2}^{b/2} \frac{db'}{b} e^{i\frac{2\pi}{a}\frac{b_x+ib_z}{b}b'} \right) \quad (21)$$

$$= -\operatorname{Re} \left((m_z - im_x) \cdot e^{i\frac{2\pi}{a}(x_0+i\frac{b_z}{2})} \left[\frac{1}{b} \frac{e^{(i\frac{2\pi}{a}\frac{b_x+ib_z}{b})b'}}{(i\frac{2\pi}{a}\frac{b_x+ib_z}{b})} \right]_{-b/2}^{b/2} \right) \quad (22)$$

$$= -\operatorname{Re} \left((m_z - im_x) \cdot e^{i\frac{2\pi}{a}(x_0+i\frac{b_z}{2})} \cdot \frac{2 \sin\left(\frac{2\pi}{a}\left(\frac{b_x}{2} + i\frac{b_z}{2}\right)\right)}{2 \cdot \frac{2\pi}{a}\left(\frac{b_x}{2} + i\frac{b_z}{2}\right)} \right) \quad (23)$$

$$= -\operatorname{Re} \left((m_z - im_x) \cdot e^{i\frac{2\pi}{a}(x_0+i\frac{b_z}{2})} \cdot \operatorname{si}\left(\frac{2\pi}{a}\left(\frac{b_x}{2} + i\frac{b_z}{2}\right)\right) \right), \quad (24)$$

which we abbreviate as $-\operatorname{Re}(A B C)$. Here $\operatorname{si} x := \frac{\sin x}{x}$. We now take into account that $\frac{\partial A}{\partial\left(\frac{2\pi}{a}x_0\right)} = \frac{\partial C}{\partial\left(\frac{2\pi}{a}x_0\right)} = 0$ and $\frac{\partial B}{\partial\left(\frac{2\pi}{a}x_0\right)} = i B$. Then the fence equations (12) and (13) can be expressed as

$$0 \stackrel{!}{=} \operatorname{Re}(i A B C) \stackrel{!}{=} \operatorname{Re}(i^2 A B C), \quad (25)$$

which is equivalent to the condition $A B C \stackrel{!}{=} 0$. As $B \neq 0$, Equation (25) is fulfilled if and only if

$$0 \stackrel{!}{=} A = m_z - im_x \quad (26)$$

or

$$0 \stackrel{!}{=} C = \operatorname{si}\left(\frac{2\pi}{a}\left(\frac{b_x}{2} + i\frac{b_z}{2}\right)\right). \quad (27)$$

The zeros of the si function are $m\pi, m \in \mathbb{Z} \setminus \{0\}$ and so the control fence transcribed in $\mathcal{T} := \mathcal{T}_{\text{LF}} \times \mathcal{T}_{\text{HF}}$ reads

$$\begin{aligned} \mathcal{F}_{\mathcal{T}} := & \{(0, m_y, 0, b_x, b_y, b_z) \mid m_y, b_x, b_y, b_z \in \mathbb{R}\} \\ & \cup \{(m_x, m_y, m_z, ma, b_y, 0) \mid b_y, H_x, H_y, H_z \in \mathbb{R}, m \in \mathbb{Z} \setminus \{0\}\}. \end{aligned} \quad (28)$$

This is exactly the control fence depicted in Figures 8 and 9. The control fence parts in \mathcal{T}_{LF} and \mathcal{T}_{HF} are independent of each other; the sliding and walking motions are *decoupled*, and we can consider the two transcription spaces separately.

3.6 Experiments: Investigation of the transport modes

3.6.1 Sliding and walking: design of control loops

As the fence equations for the stripe pattern decouple to independent equations for the low- and high-frequency fields, the fence components are orthogonal to each other and induce different transport modes. Winding around a low-frequency fence (in \mathcal{T}_{LF}) with fixed biped vector (in \mathcal{T}_{HF}) leaves the orientation of the rod invariant and leads to the mentioned sliding motion. Winding around a high-frequency fence (in \mathcal{T}_{HF}) with fixed biped magnetic moment (in \mathcal{T}_{LF}) leaves the single-particle potential landscape invariant and causes the walking motion. As the calculation has shown that there are no more fence components, we can conclude there are also no more transport modes; each topologically non-trivial adiabatic transport in this system can be written as a composition of a sliding and a walking motion. In order to probe the predictions from simulation and theory, it has hence suggested itself to start the experiments trying to realize these two transport modes separately.

Figures 11 and 12 show the applied control loops after transcription in the low- and high-frequency transcription spaces. While the colors represent different rod lengths from red (b_1) to magenta (b_8), the change in lightness, as in Section 2.3, indicates the changing control parameter.

3.6.2 Sliding and walking: results

Sliding Figure 11 shows the transcribed low-frequency control loops applied in the sliding experiments; the high-frequency field was left at fixed direction parallel to the stripes, as in the simulation from Figure 5. The low-frequency loops by design just wind around the single red fence line. This means that the theory predicts all rods should slide one lattice constant per loop, independently of their length. As the loops are driven counterclockwise, the rollig wheel rule tells us that the rods will be sliding to the left.

The experiments confirm this prediction. One characteristic result for the sliding motion is depicted in Figure 13, which is based on Video 3: All rods indeed slide to the left with a speed of one lattice constant per loop, independent of their length. The figure shows the particles as well as their trajectories within a time interval of $2T = 40$ s (visible thanks to a digitally made “long exposure” effect).

Their equal speed becomes evident from Figure 14: It shows a “long-exposure photo from the comoving frame of reference”. I. e., a projection of the entire¹⁴ video along the $x + at/T$ axis, parallel to which the spacetime trajectories (“world lines”) of the rods are claimed to be. That the rods almost

¹⁴However only with frames stroboscopically captured in discrete time intervals T . In this way, in each frame the external field is the same.

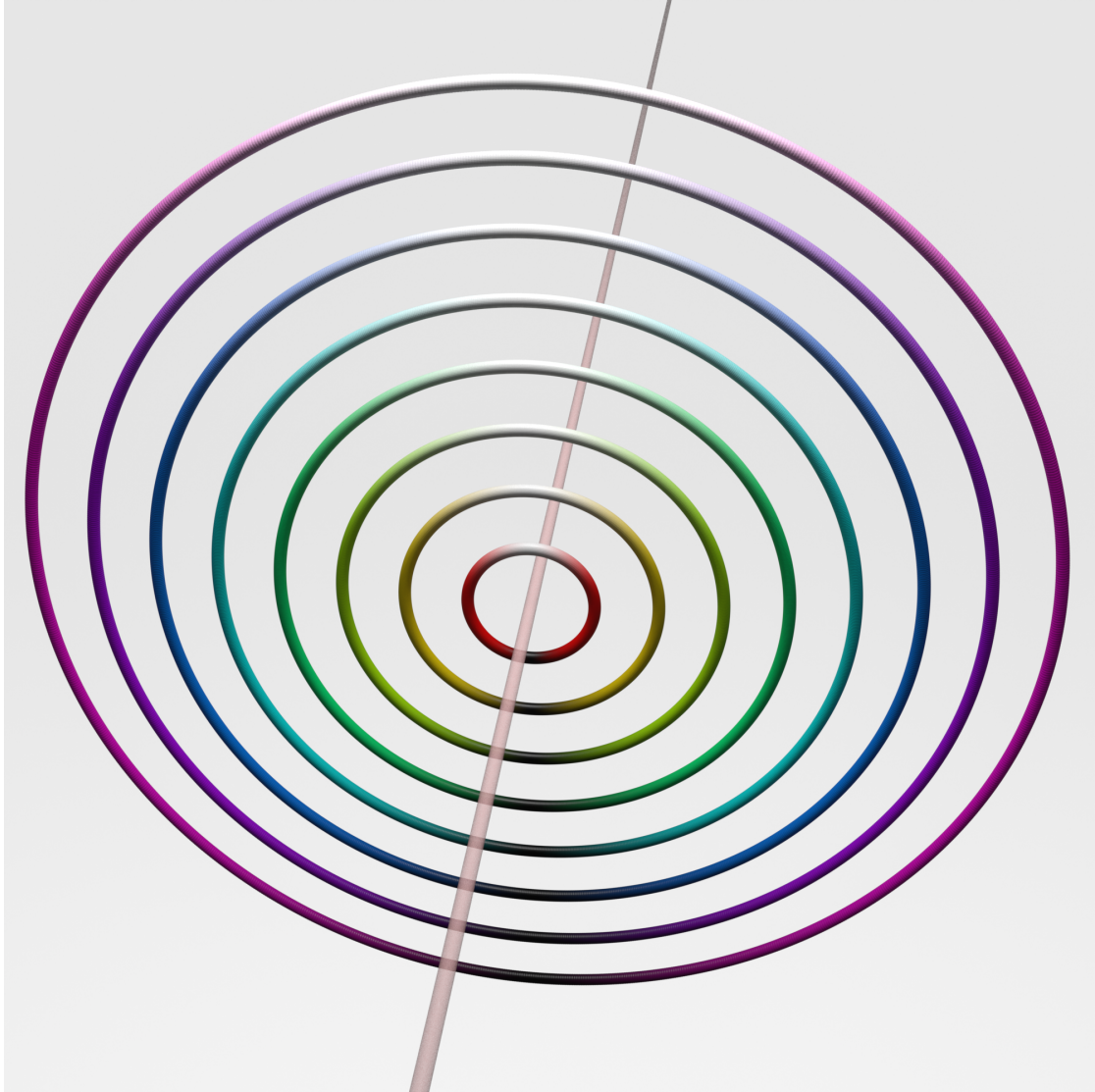


Figure 11: Control loops in the low-frequency transcription space \mathcal{T}_{LF} . The coordinate system is the same as in Figure 8, but is omitted here for better visibility of the loops. The different radii and colors represent different rod lengths from b_1 (red) to b_8 (magenta), the changing lightness indicates the control parameter. The loop was driven in counter-clockwise direction. For any rod length, it winds around the fence once and thus is predicted to induce a sliding motion by one lattice constant to the left. For the experimental results, see Figures 13 and 14.

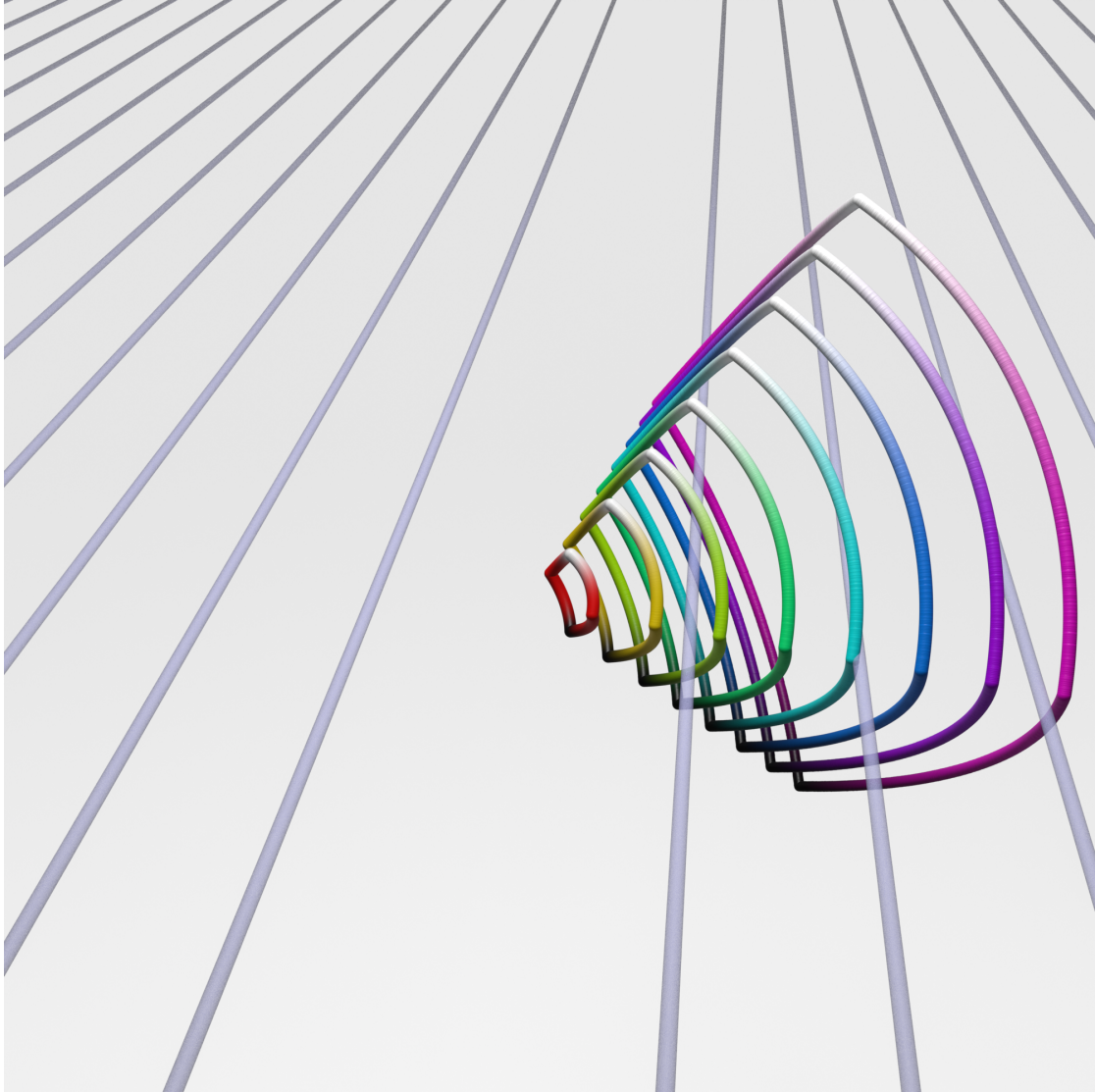


Figure 12: Control loops in the high-frequency transcription space \mathcal{J}_{HF} . The coordinate system is the same as in Figure 9, but is omitted here for better visibility of the loops. The different radii and colors represent different rod lengths from b_1 (red) to b_8 (magenta), the changing lightness indicates the control parameter. The loop was driven clockwise. For lengths b_1 and b_2 , the loop winds around no fence segment and is thus predicted to induce no transport. The b_3 and b_4 loops wind around one segment and therefore should make those bipeds walk one lattice constant, b_5 should walk one or two (not clear from theory as the loop cuts the fence), b_6 and b_7 two, and b_8 three. For the experimental results, see Figures 15 and 16.

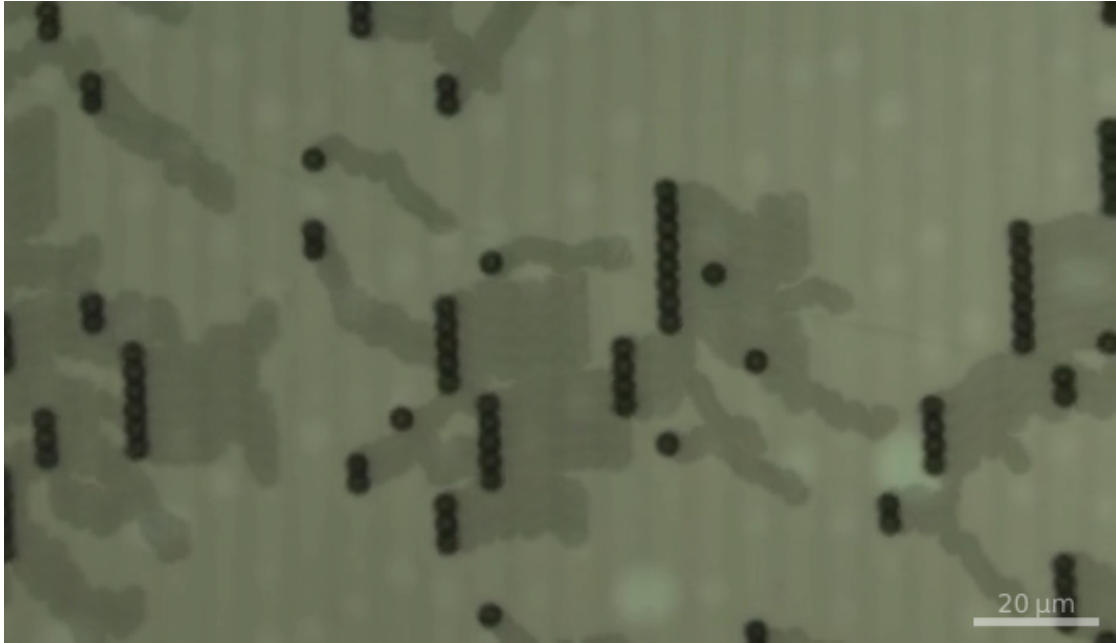


Figure 13: Typical experimental result for the sliding motion. The figure consists of the overlaid frames in the first 3 s of Video 3 (accessible via the QR code). In this time, the low-frequency control loop from Figure 11 is driven three times while the high-frequency field keeps the bipeds oriented along the stripes. As predicted, all single particles and bipeds slide to the left with a speed of one lattice constant per loop, independent of their length. This becomes more evident from Figure 14.



aren't smeared out here shows that they are indeed moving with velocity $-\frac{a}{T}$ in x direction.

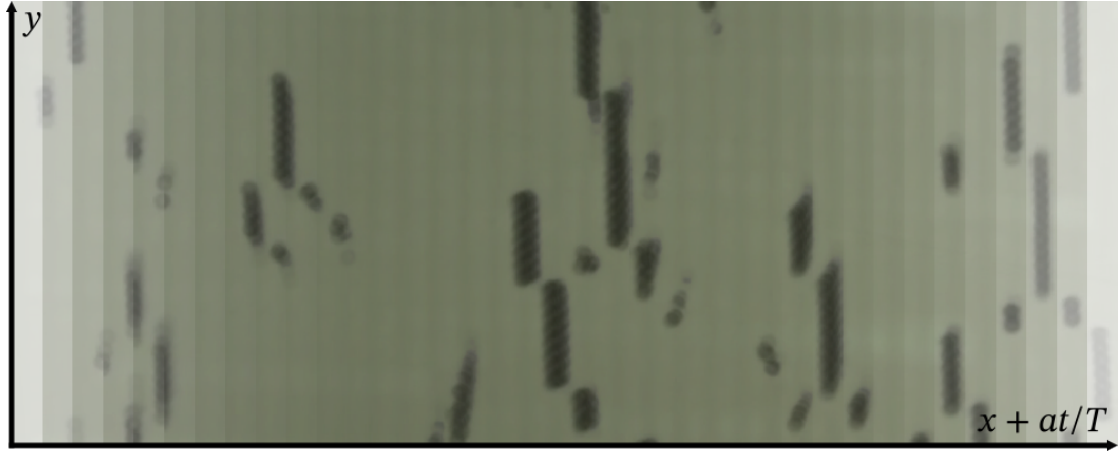


Figure 14: Projection of Video 3, showing that all rods slide with equal speed. Technically, this figure is an overlay of video frames stroboscopically captured at times $t_i = t_0 + iT, i \in \{1, \dots, 14\}$ with T the loop duration. Each frame is shifted to the right with respect to the preceding one by one lattice constant a .

Walking Now, for the walking experiments, the magnetic moments \mathbf{m}_n were kept constant and pointing upwards perpendicular to the pattern, as in the simulation from Figure 6. The applied high-frequency control loops are visible in Figure 12. As opposed to the sliding experiments, here different transcribed control loops wind around different numbers of fence segments, which means theory predicts bipeds to walk with different speeds depending on their length. In particular, bipeds of lengths b_1 and b_2 are predicted not to walk forward, $b_{3,4}$ should walk one lattice constant per loop, b_5 one or two lattice constants (not clear as loop cuts fence), $b_{6,7}$ two lattice constants and b_8 three lattice constants. The direction will be to the right according to the rolling wheel rule.

Figure 15 shows a corresponding experiment, based on Video 4. In the video we can see a single biped walking to the right. On its way there are single particles that don't move forward but are incorporated by the biped, which becomes longer in this way and moves with increasing step size and speed. We can also observe in the video that the rod always steps on the gray stripes, like in the simulation. In the Figure, an overlay analogous to Figure 13, these details are hard to recognize but we can at least see that the biped is moving to the right, in agreement with the rolling wheel rule, and that the single particles don't move.



Figure 15: Typical experimental result for the walking motion. The figure consists of the overlaid frames in the first 5 s of Video 4 (accessible via the QR code). In this time, the low-frequency control loop from Figure 12 is driven five times while the low-frequency field is fixed pointing upwards. As predicted, single particles don't move forward and the biped moves to the right. More details are visible in the video and in Figure 16.

Again, a second graphics quantifies the observations: Figure 16 shows projections of the video of the walking motion along y (bottom) and along t direction (top). In the lower part, we see the moving rods as lines colored according to their length. Each vertex where two lines join corresponds to a joining event of two rods, or, in this case, a rod and a single particle. The kinks in the lines arise on the dark (gray) stripes because each rod always has one foot there; additionally, as they show the T -periodicity, they allow us to read the step size of each rod and confirm that (in the absence of joining events) $b_{3,4}$ walk one, $b_{5,6,7}$ two and b_8 three lattice constants per step. In particular, the b_5 biped seems to behave as if the fence segment cut by the loop lied *inside* the loop. These movements are in agreement with the theoretical prediction.

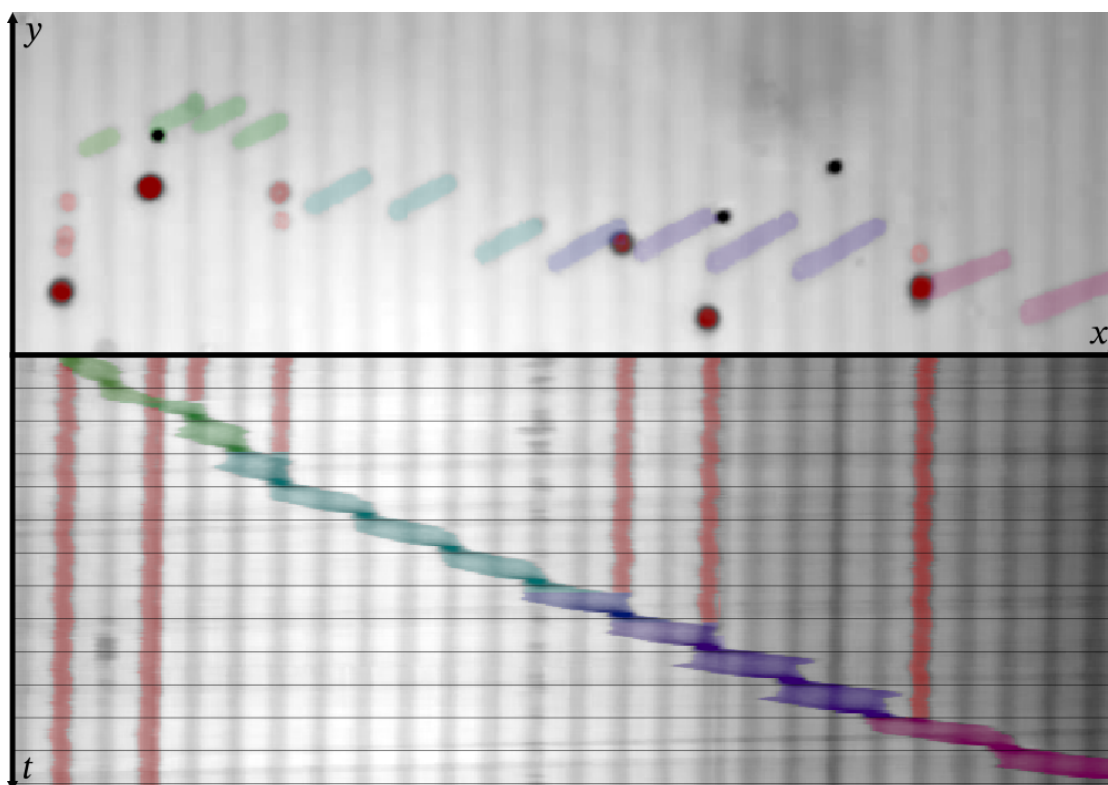


Figure 16: Projections of Video 4 along the y (top) and the t axis (bottom). The bottom part shows the different walking speeds of rods with different lengths. For easier visualization, the lower part of this figure contains all frames whereas the upper part only consists of stroboscopically captured frames as in Figure 14.

3.6.3 Treadmill and dancing

Instead of keeping one of the fields fixed, it is also possible to modulate both field directions. So I have combined a walking and a sliding motion with opposite transport directions (see Figure 17 and Video 5): While all assemblies slide to the left at one lattice constant per loop, the walking speed to the left monotonically increases with the rod length. So rods of lengths $b_{1,2}$ slide to the left, those with lengths $b_{3,4}$ walk in place (like humans running on a treadmill or on an escalator in the wrong direction) and longer ones walk to the right.



Figure 17: Typical experimental result for the treadmill motion. The figure consists of the overlaid frames from $t = 12.4$ s to 15.4 s of Video 5 (accessible via the QR code). In this time, the low-frequency control loop from Figure 11 is driven three times counter-clockwise while the high-frequency control loop from Figure 12 is driven three times clockwise. In agreement with the theory, single particles and bipeds of length b_2 slide to the left (e. g. ① and ②), bipeds $b_{3,4}$ walk in place (e. g. ③ and ④) and longer ones walk to the right (e. g. ⑤).

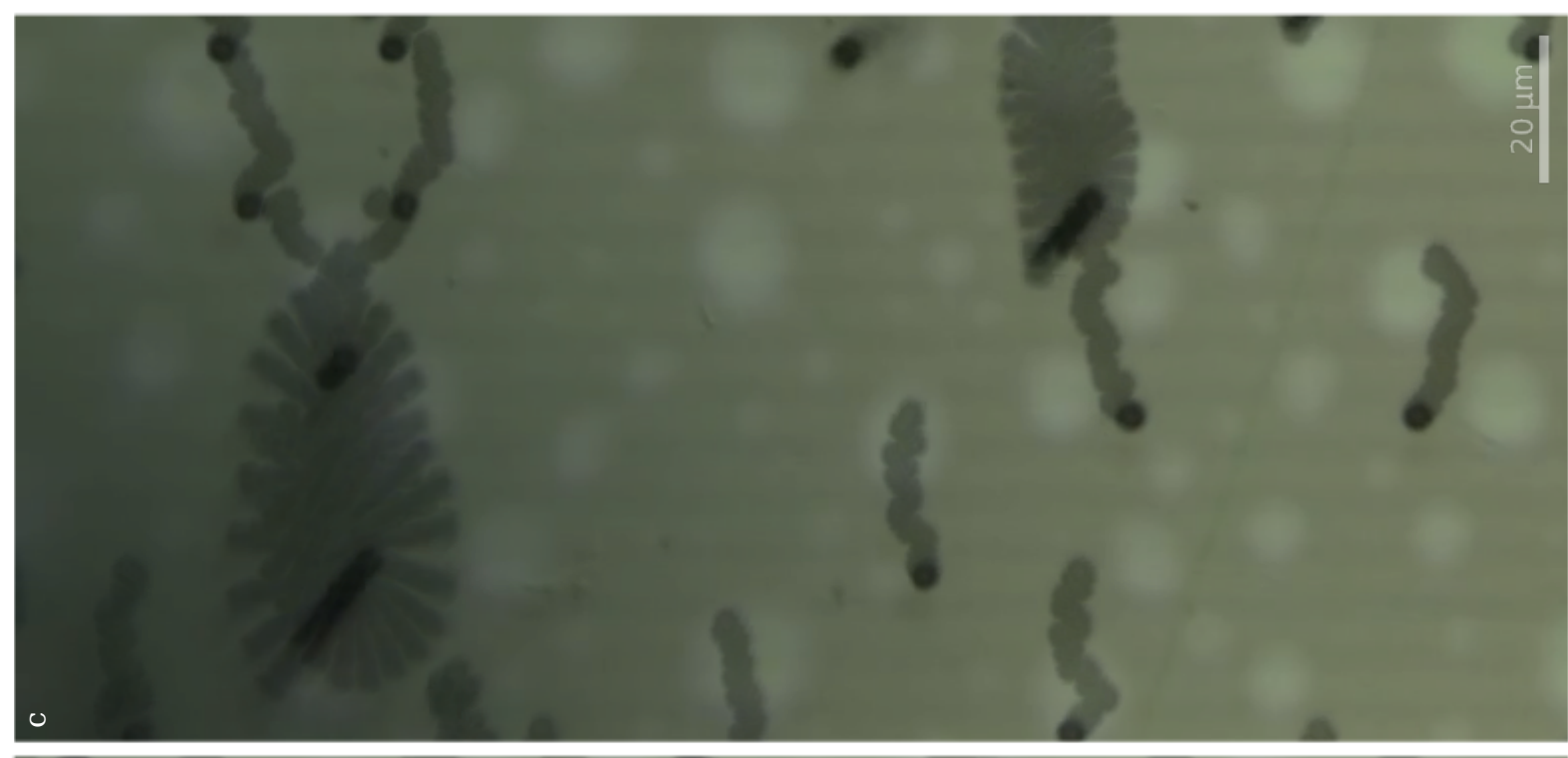
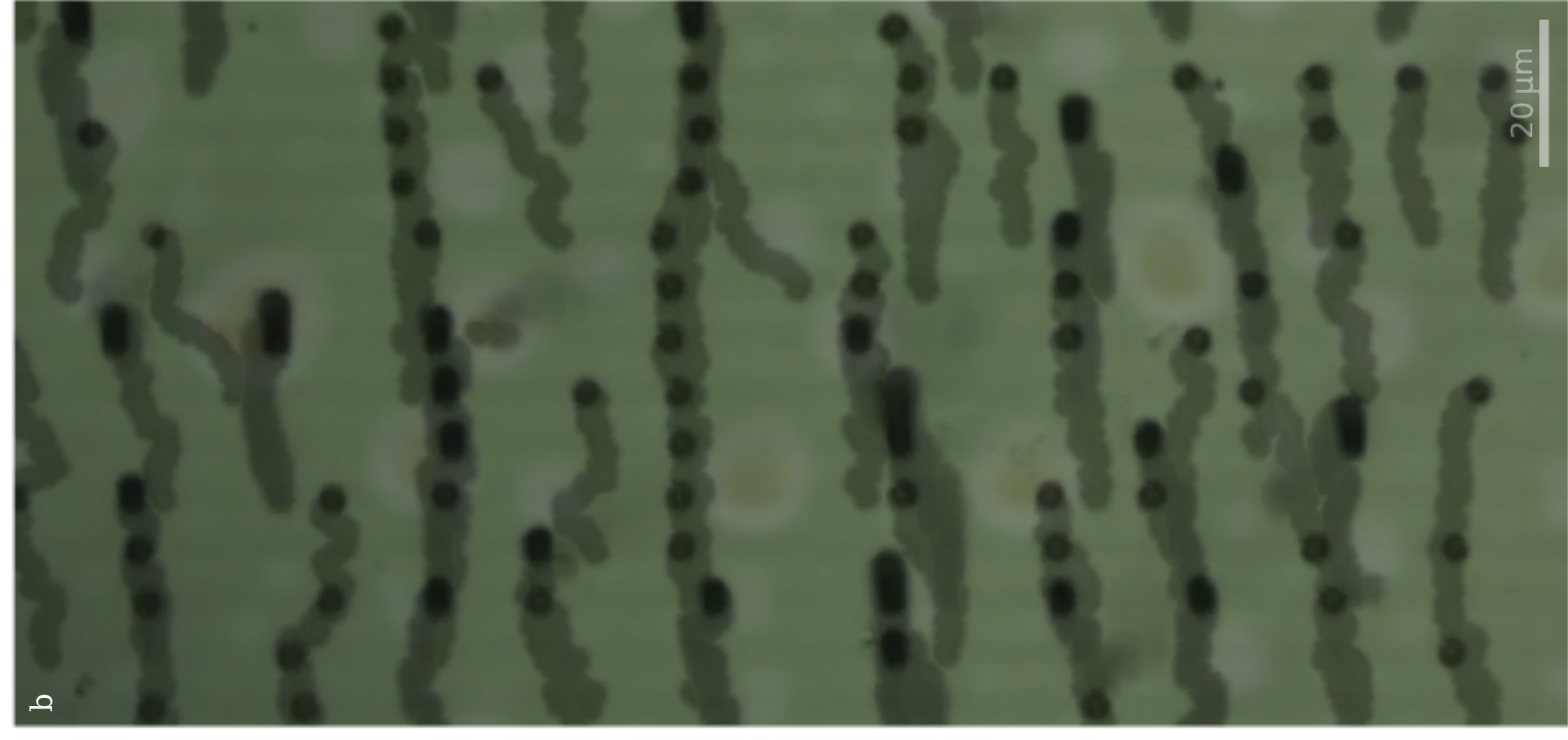
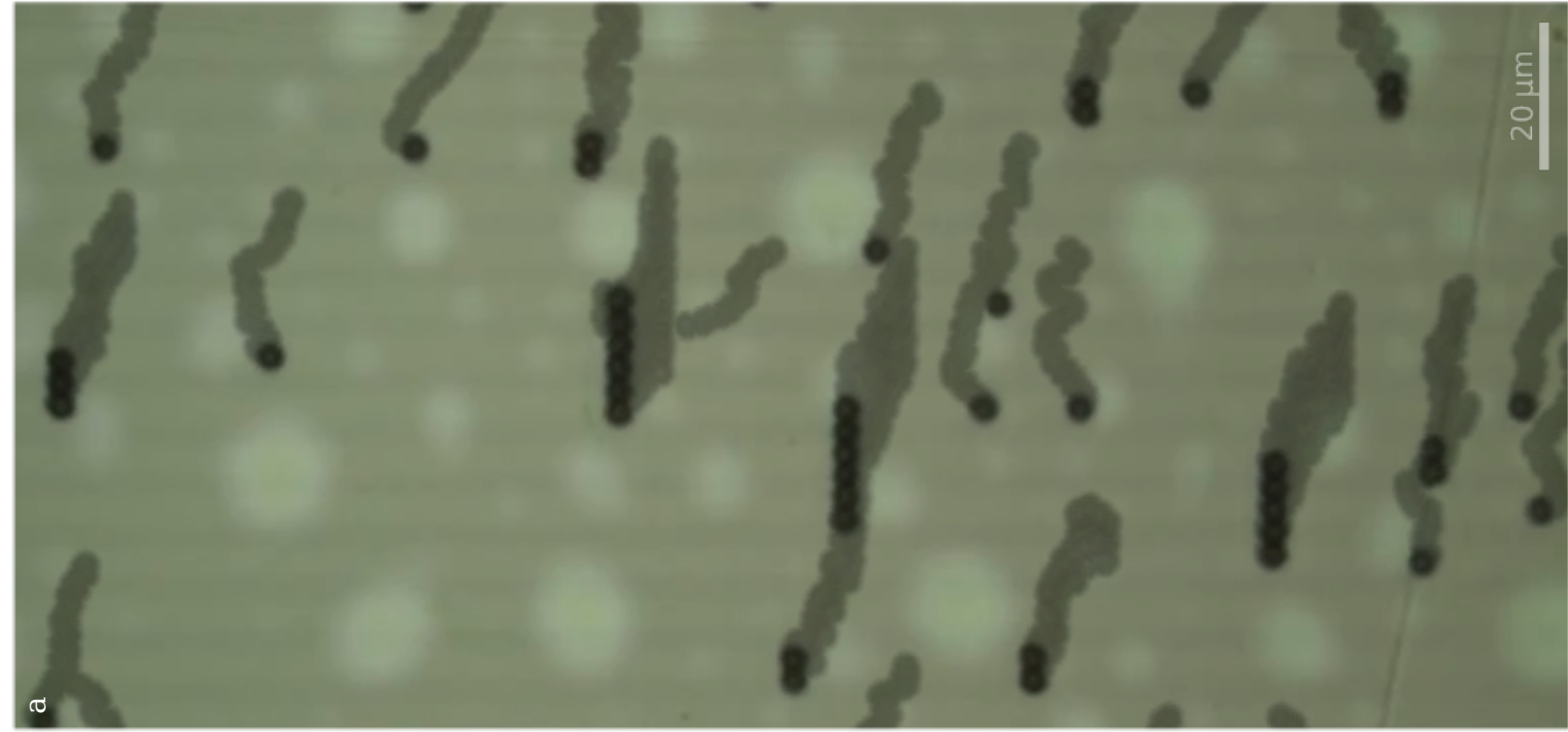


For the sliding motion, many more variations are possible; Figure 18 and Video 6 show three of them. A first possibility is to let bipeds slide with different fixed orientations, which we describe by the polar and azimuthal angles Θ and Φ in spherical coordinates. In the left part of Figure 18 and Video 6 we see an experiment where the bipeds are lying flat and longitudinally to the sliding direction ($\Theta = 90^\circ$, $\Phi = 0^\circ$). In the middle part of Figure 18 and Video 6, they have an out-of-plane orientation ($\Theta = 40^\circ$, $\Phi = 12^\circ$) and slide to the right, as the sliding loop in Figure 11 is driven clockwise. Finally, another way of combining two modulations is shown in the right part of Figure 18 and Video 6: All bipeds are sliding to the left while rotating around one of their ends (like humans dancing on a carnival float). In contrast with the treadmill motion, here the orientation modulation does not cause any movement as the high-frequency control loop winds around no fence.

All these - partly dancing-like - movements are possible because the sliding motion works independently of the biped orientation. Conversely, theory predicts that also the walking motion should work independently of the low-frequency field orientation: For any fixed orientation of \mathbf{H}_{LF} , the rods should walk with the same speed. The difference should just be whether the rods step on gray stripes, green stripes or gray-green edges. This remains to be tried in future experiments, and there is also room for other agile biped movements which we haven't observed until now.

Figure 18 (see page 38): Sliding experiments with different biped orientations. In all cases the low-frequency loop from Figure 11 with period $T = 20$ s was used, but each time with a different high-frequency loop. (a) Sliding while keeping the high-frequency field and thus the rod orientation parallel to the sliding direction ($\Theta = 90^\circ$, $\Phi = 0^\circ$). (b) Sliding with fixed out-of-plane high-frequency field and rod orientation ($\Theta = 40^\circ$, $\Phi = 12^\circ$). Here the rods slide to the right because the loop was driven clockwise. (c) Sliding with simultaneous in-plane rotation of the rods ($\Theta \approx 90^\circ$, Φ changing with constant angular velocity $\frac{2\pi}{T}$). The figures are overlays of the frames from the first 2 s of Video 6.





4 First order, or: how to break and glue

4.1 Experimental result: dividing bipeds

On our way to achieve agile particle movement, so far we have – controlling the foothold on the substrate and the orientation of agile bipeds – been able to reproduce a sliding and a walking motion and combinations of them. A third possible way of moving is moving by shape changes, which has not occurred in the experiments shown up to this point.

However, as visible for example in Figure 16, often the assembly of shorter bipeds to longer ones is observed. On the contrary, the inverse process – division of longer bipeds into shorter ones – practically never happens in experiments. This can be explained with the high binding energy of the particles due to the high-frequency field, as described by equation (11) on page 22.

In order to make the division of bipeds into bipeds possible, and so gain greater control over the actual shape of our assemblies, we (that is, Anna Rossi and me) used a different pattern which should act like an ax and break bipeds into two parts.

The pattern, developed and used in Anna’s PhD [7], is visible in Figure 19: It consists of a square pattern which is locally deformed around a boat-shaped region in the center [8, p. 4]. This region is *cloaked* for single particles because they, if moving from the bottom left to the top right in the picture (or vice versa), don’t enter the boat but move around it.¹⁵ At the cusps of the cloaked region, indicated by the white spots in Figure 19, incoming particles will either go to the left or to the right.

What we then did is let a rod slide with its long side hitting such a cusp in order use the cloaked region as blade of the ax, splitting the incoming biped into two parts. We used a sliding loop as in Section 3.6.2.¹⁶

In this experiment we were indeed able to observe rod divisions, as the example in the inset of Figure 19 shows. Like other division events it happened near, but not exactly at the cusp of the blade. We explain this by a local increase of the magnetic energy of the assembly, caused by the deformed pattern under it.

¹⁵Thereby their trajectories are deformed compared to the ones on a standard square pattern only around the cloak, so that far away from the cloak they coincide with the original trajectories.

¹⁶This works because the square pattern is a superposition of two orthogonal stripe patterns with a potential of the form $U_4(x, y) = U_2(x) + U_2(y)$, and $U_2(x)$ equal to the stripe pattern potential (24). Therefore the square pattern fence is a superposition of two copies of the stripe pattern fence, rotated with respect to each other around the z axis by $\frac{\pi}{2}$.

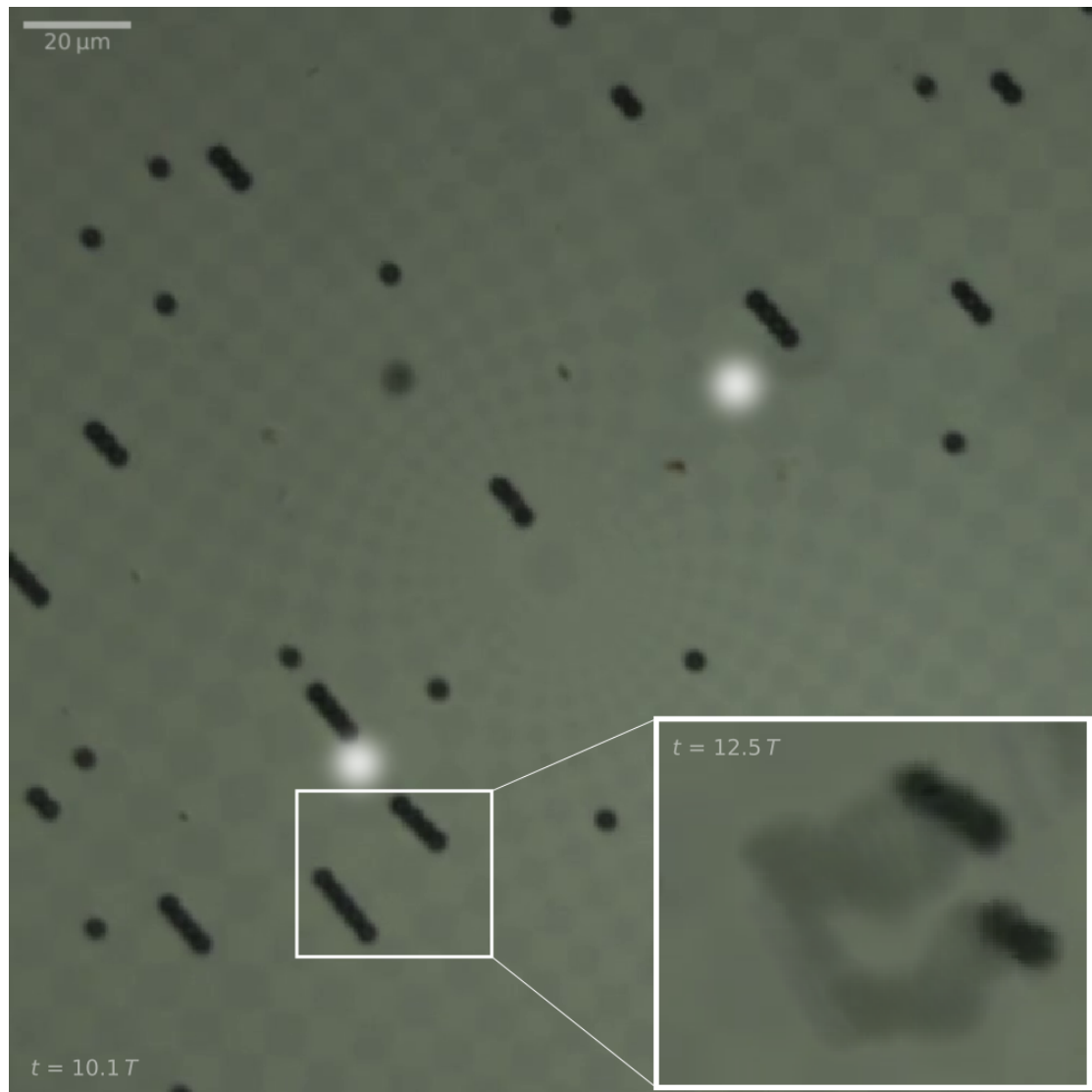


Figure 19: Division experiment, based on Video 7 (accessible via ). Here the particles are placed on a square pattern with a boat-shaped cloaked region, as developed and used in [7]. The bipeds were driven by a sliding loop with $T = 10$ s while their orientation was kept fixed transverse to the sliding direction. The cloaked region has two cusps; their approximate positions are drawn as white spots (manually added to the picture). The inset shows a rod division near one of the cusps of the cloaked region.

4.2 Lessons from the parameter studies

Unlike the walking and sliding motion, the division is not an adiabatic process, which explains why we found that experimental parameters have a big influence on whether this process works or not, and that also randomness plays a role here. On the way to the above result we have therefore studied the influence of the parameters, which provided us with a deeper understanding of the dynamical behavior of our system. I will summarize our results here, also as a reference for future experiments.

To be able to divide in a controlled manner, the bipeds have to hit the blade with a point close to their center (otherwise they will just go around it. This means they should be

1. sufficiently long, thin and straight, which requires a sufficiently strong particle-particle attraction, i. e. a *low* $\frac{H_{LF}}{\tilde{H}_{HF}}$ ratio;
2. sufficiently fragile and sensitive to the pattern, which requires a sufficiently weak particle-particle and a high particle-substrate interaction, i. e. a *high* $\frac{H_{LF}}{\tilde{H}_{HF}}$ ratio.

It is hence not guaranteed that there is a suitable $\frac{H_{LF}}{\tilde{H}_{HF}}$ ratio fulfilling both conditions, and indeed it was challenging to observe such a splitting event. In our attempts to there we have studied the influence of numerous parameters such as

- the lattice constant (smaller lattice constants leads to longer rods),
- the cloak size (bipeds tend to cross smaller cloaks, and to get caught at the cusps of bigger cloaks),
- the high-frequency modulation function, replacing $\cos(\omega_{HF}t)$ in Equation (3) on page 13 (a rectangular function $\text{sign}(\cos(\omega_{HF}t))$ makes the particle-particle attraction (11) twice as strong) and
- the exact loop path (a smaller/larger control loop in \mathcal{C}_{LF} leads to weaker/stronger forces and propulsion).

Also the cloak shape (boat or ellipse) affects the bipeds' tendency to cross the cloak or get caught.

What in the end led to the successful experiment from Figure 19 and Video 7 was periodically switching between two loops - sliding and *stretching* - each fulfilling just one of the above conditions: While driving the sliding loop, the $\frac{H_{LF}}{\tilde{H}_{HF}}$ ratio was risen to 0.6 to facilitate the breaking of the bipeds. This had the drawback that with the time the bipeds deformed to non-rod-shaped clusters. Therefore, after each two sliding loops, we drove

one stretching loop with keeping both \mathbf{H}_{LF} and $\tilde{\mathbf{H}}_{HF}$ fixed at their current orientations, but decreasing their ratio to 0.1. This small pause helped the corrupted bipeds to recover into their elongated shape.

4.3 Outlook: joining bipeds

In the course of the experiments Thomas, Anna and me arrived expecting that the process of joining two bipeds together in a controlled manner might be achievable more easily than splitting them. Because, it doesn't require the fragility of the bipeds. Just two bipeds must be placed at opposite sides of the cloak such that they will meet, and join, at some later point. Nonetheless, for this to work, the particle-substrate interaction must still be strong enough for both rods to be transported over the pattern reliably, and not miss out any step (which would bring them out of synchronization). Pre-experiments suggest that the joining will work once this issue is solved, so this direction seems worth taking.

5 Higher orders, or: how to change

We have seen that already shape changes of rods are challenging to control, so it is probably even more challenging for non-rod-shaped colloidal assemblies. These would however be particularly interesting because they can presumably perform more complex shape changes. A possible solution is to investigate the effect of these shape changes in a statistical manner.

Non-rod-shaped assemblies were also created in this work, however by inducing isotropical instead of directed attraction between the particles. To this end, no oscillating but a rotating high-frequency field was used. This means we have applied the external field

$$\mathbf{H}_{\text{ext}}(t) = \mathbf{H}_{\text{LF}}(t) + \tilde{H}_{\text{HF}}(\hat{\mathbf{x}} \cos(\omega_{\text{HF}}t) + \hat{\mathbf{y}} \sin(\omega_{\text{HF}}t)), \quad (29)$$

here with $\frac{H_{\text{LF}}}{\tilde{H}_{\text{HF}}} = 0.2$, $\omega_{\text{HF}} = 2\pi \cdot 20 \text{ Hz}$ and $\hat{\mathbf{x}}$ and $\hat{\mathbf{y}}$ the unit vectors in x and y direction. A result is shown in Figure 20 and Video 8.

We see the single particles are re-assembling at specific times or values of the control parameter. This results to shape changes of the assembly, which here seem to lead to a forward displacement. The forward displacement is recognizable by the fact the assembly moves faster than the single particles (otherwise it would not be able to hunt and eat them). We call this transport mode *swimming*, even though it is not clear at this point whether hydrodynamic effects play a role here.

Shape changes were generally observed. However they were not controllable and did not always lead to a forward displacement, but also to backward or no displacement. So the aim of a future project will be finding a control parameter which, via transcription to the shape, is coupled to the displacement of the assembly - perhaps similar as described by Alfred Shapere and Frank Wilczek, who have also related shape changes and swimming motion to a loop in an abstract space [9, p. 558]. This will most probably be the starting point of the continuation of the present Master's project.

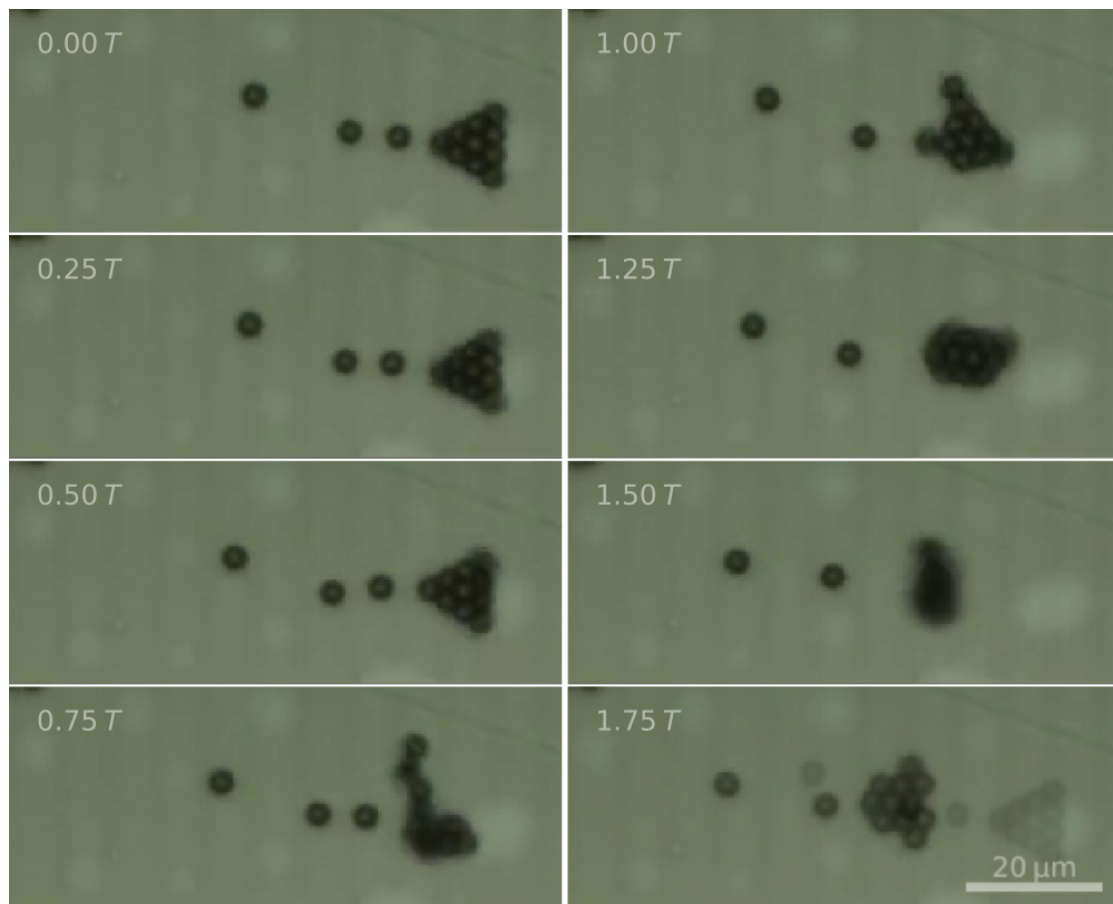


Figure 20: Swimming experiment. The Figure shows snapshots from the initial part of Video 8 (accessible via QR code), taken at intervals of a quarter-period $\frac{1}{4}T$ with $T = 20$ s. For comparison, the last snapshot is overlaid with a shadow of the first. The low-frequency loop was the sliding loop from Figure 11; the high-frequency field was not oscillating as in the other experiments but rotating in-plane with frequency 20 Hz. One can see single particles as well as a non-rod-shaped cluster, all moving to the left. Within each period the clustered particles detach and re-assemble, which leads to a deformation and propulsion of the assembly. The latter is recognizable at the fact that the cluster moves faster than the single moves faster, allowing it to incorporate one and to catch up with the others. The depicted event was chosen intentionally to illustrate the effect; shape changes of clusters occurred in general but their precise course seemed arbitrary.

6 Discussion and outlook

In this Master thesis I have, building upon previous works by Mahla, Anna and Adrian, investigated ways to control shape and motion of paramagnetic colloidal assemblies on a ferromagnetic pattern. I used simulation, theory and experiment. The new aspect I introduced was replacing the former strong adiabatically modulated external magnetic field by a superposition of a strong high-frequency magnetic field and a weak low-frequency magnetic field. My experiments have shown that the former then completely determines the magnetic dipolar particle-particle interaction whereas the latter is solely responsible for the substrate-particle interaction. My calculation of the fence in the high- and low-frequency transcription spaces then has shown this leads to a decoupling of two modes of topological transport - walking and sliding. This description could in principle be applicable to other walking- or sliding-like motions on periodically patterned substrates, as of humans on stairs, ladders or escalators.

The motion of these agile bipeds being exhausted completely, together with Anna I have moved on to real shape changes - trying to divide or join bipeds in a controlled manner with a cloaking pattern. These experiments have worked partially and taught us a lot about the non-adiabatic behavior of the system: First, the binding is quite irreversible, and so biped joining can probably be achieved more easily than dividing. Second, randomness plays a big role here and so it seems statistical methods need to be applied.

Both mentioned points contain opportunities for future experiments. Exhausting the randomness was already part of some late Master thesis experiments of mine, where I used a non-oscillating but rotating high-frequency field to build different non-rod-shaped assemblies. Upon sliding, they performed periodic random shape changes that were correlated to propulsion. Phenomena like this are known from swimmers at low Reynolds numbers which are also given here. In addition, still the particles and assemblies are moving in a discrete environment which simplifies the theoretical description enough to (hopefully) find a relation between magnetic field, shape change and motion.

This will probably be the starting point for my continuation of this project in the PhD. I enjoyed this Master's project very much, and I'm happy having worked with a system accessible by all simulation, theory and experiment - the results of which finally converged and contributed to a deeper understanding.

7 Acknowledgements

It's impossible anyway to thank every person here that I would like to, so I will do that directly and for instance just acknowledge the most prominent contributions of those who were directly involved in this project.

Thank you, Thomas Fischer, for your very good ideas (such as the field oscillation, field rotation and the ax), your supervision well-balanced between guidance and letting-do, for your patient support during the writing phase, and for the review of this thesis.

Thank you, Anna Rossi, for continuously supporting me in the easier and less easy times during this project (and before), for showing me a new level of doing experiments, and for proof-reading this thesis.

Thank you, Adrian Ernst, for your reliable availability and your well-founded advice how to put the experimental system into your simulation software.

Thank you, Daniel de las Heras, for discussing with me the fence calculation, and for reviewing this thesis.

Thank you, Aneena Rinu Perayil, Farzaneh Farrokhzad, Laurens Wittmann, Max Pöhlmann, Sebastian Wohlrab and Thomas Märker, for our lab, computer, and whiteboard discussions.

Thank you, Christine Linser, for your always friendly and helpful support in organizational and personal matters.

Thank you, Benjamin Elschner, for the design consulting for this thesis.

8 Erklärung/Declaration

Hiermit erkläre ich, dass ich die vorliegende Arbeit selbstständig und ohne Benutzung anderer als der angegebenen Hilfsmittel angefertigt habe. Originaldaten sind auf Anfrage verfügbar. Alle Stellen, die wörtlich oder sinngemäß aus veröffentlichten oder nicht veröffentlichten Schriften entnommen wurden, sind als solche kenntlich gemacht. Die Arbeit habe ich in gleicher oder ähnlicher Form nicht bereits zur Erlangung eines akademischen Grades eingereicht.

I hereby declare that I have completed this thesis independently and without using any tools other than those specified. Original data are available upon request. All passages taken literally or analogously from published or unpublished writings are marked as such. I have not already submitted the work in the same or a similar form to obtain an academic degree.

20.03.2025
Jonas Elschner

References

- [1] Jonas Elschner, Farzaneh Farrokhzad, Piotr Kuświk, Maciej Urbaniak, Feliks Stobiecki, Sapida Akhundzada, Arno Ehresmann, Daniel de las Heras, and Thomas M. Fischer. “Topologically controlled synthesis of active colloidal bipeds”. In: *Nature Communications* 15.1 (July 9, 2024), p. 5735. ISSN: 2041-1723. DOI: 10.1038/s41467-024-50023-7. URL: <https://www.nature.com/articles/s41467-024-50023-7> (visited on 09.02.2025).
- [2] Adrian Ernst. “Simulation of Topological Transport of Colloidal Particle Assemblies above Magnetic Patterns”. PhD thesis. University of Bayreuth, 2023. DOI: 10.15495/EPUB_UBT_00006879. URL: <https://epub.uni-bayreuth.de/id/eprint/6879> (visited on 12.01.2025).
- [3] Adrian Ernst, Anna M. E. B. Rossi, and Thomas M. Fischer. “Adiabatic and irreversible classical discrete time crystals”. In: *SciPost Physics* 13.4 (Oct. 11, 2022), p. 091. ISSN: 2542-4653. DOI: 10.21468/SciPostPhys.13.4.091. URL: <https://scipost.org/10.21468/SciPostPhys.13.4.091> (visited on 12.01.2025).
- [4] Johannes Loehr, Daniel de las Heras, Michael Loenne, Jonas Bugase, Adam Jarosz, Maciej Urbaniak, Feliks Stobiecki, Andreea Tomita, Rico Huhnstock, Iris Koch, Arno Ehresmann, Dennis Holzinger, and Thomas M. Fischer. “Lattice symmetries and the topologically protected transport of colloidal particles”. In: *Soft Matter* 13.29 (2017), pp. 5044–5075. ISSN: 1744-683X, 1744-6848. DOI: 10.1039/C7SM00983F. URL: <https://xlink.rsc.org/?DOI=C7SM00983F> (visited on 09.01.2025).
- [5] Mahla Mirzaee-Kakhki, Adrian Ernst, Daniel de las Heras, Maciej Urbaniak, Feliks Stobiecki, Jendrik Gördes, Meike Reginka, Arno Ehresmann, and Thomas M. Fischer. “Simultaneous polydirectional transport of colloidal bipeds”. In: *Nature Communications* 11.1 (Sept. 16, 2020), p. 4670. ISSN: 2041-1723. DOI: 10.1038/s41467-020-18467-9. URL: <https://www.nature.com/articles/s41467-020-18467-9> (visited on 12.01.2025).
- [6] Mahla Mirzaee-Kakhki, Adrian Ernst, Daniel de las Heras, Maciej Urbaniak, Feliks Stobiecki, Andreea Tomita, Rico Huhnstock, Iris Koch, Arno Ehresmann, Dennis Holzinger, and Thomas M. Fischer. “Gauge invariant and gauge dependent aspects of topological walking colloidal bipeds”. In: *Soft Matter* 17.6 (2021), pp. 1663–1674. ISSN: 1744-683X, 1744-6848. DOI: 10.1039/D0SM01670E. URL: <https://xlink.rsc.org/?DOI=D0SM01670E> (visited on 09.01.2025).
- [7] Anna M. E. B. Rossi. “Effect of Perturbations on the Transport of Particles on Magnetic Patterns”. PhD thesis. University of Bayreuth, 2025.

DOI: 10.15495/EPUB_UBT_00008049. URL: <https://epub.uni-bayreuth.de/id/eprint/8049> (visited on 10.03.2025).

- [8] Anna M. E. B. Rossi, Thomas Märker, Nico C. X. Stuhlmüller, Piotr Kuświk, Feliks Stobiecki, Maciej Urbaniak, Sapida Akhundzada, Arne J. Vereijken, Arno Ehresmann, Daniel de las Heras, and Thomas M. Fischer. “Topologically cloaked magnetic colloidal transport”. In: *Nature Communications* 16.1 (Feb. 20, 2025), p. 1828. ISSN: 2041-1723. DOI: 10.1038/s41467-025-57004-4. URL: <https://www.nature.com/articles/s41467-025-57004-4> (visited on 28.02.2025).
- [9] Alfred Shapere and Frank Wilczek. “Geometry of self-propulsion at low Reynolds number”. In: *Journal of Fluid Mechanics* 198.-1 (Jan. 1989), p. 557. ISSN: 0022-1120, 1469-7645. DOI: 10.1017/S002211208900025X. URL: http://www.journals.cambridge.org/abstract_S002211208900025X (visited on 19.01.2025).